MICROBIAL PHYSIOLOGY AND BIOSIGNATURE PRODUCTION:

MINERALOGICAL, MORPHOLOGICAL AND GEOCHEMICAL EXAMPLES

A Dissertation

by

ZHIRUI ZENG

Submitted to the Office of Graduate and Professional Studies of
Texas A&M University
in partial fulfillment of the requirements for the degree of

DOCTOR OF PHILOSOPHY

Chair of Committee,	Michael M. Tice
Committee Members,	Michael Pope
	Franco Marcantonio
	Paul Straight
Head of Department,	John R. Giardino

December 2014

Major Subject: Geology

Copyright 2014 Zhirui Zeng

ABSTRACT

Microbial processes have driven biogeochemical cycles and modified the Earth's surface throughout geologic time. Some microbial physiologies created unique chemo-physical conditions to influence mineral precipitation and trace element cycling. Such physiology-specific products may be preserved as long-lived biosignatures in the geologic record and could be used as a new evidence to detect ancient life.

Microbial iron reduction is one of the most important geobiochemical process in nature and can promote carbonate precipitation. However, little is known about how iron reducing bacteria induce carbonate formation, and control carbonate composition and morphology. Direct observation and geochemical modeling indicated actively metabolizing cells locally raised *p*H and provided essential nucleation sites for carbonate precipitation. By altering metal ion concentrations around cell surfaces, and inducing metastable carbonate, iron reducing microorganisms could produce a wide range of carbonate cements in natural sediments.

In addition, iron reducing bacteria can use diverse physiologies (membrane bound enzymes, soluble electron shuttles, and nanowires) to transfer electrons to insoluble iron oxide minerals. This physiologies may create a variety of physicochemical microenvironments in which mineral dissolution and precipitation can occur. The incubation of *S. oneidensis MR-1*, *G. fermentans,* and *G. metallireducens GS-15*, representing three different physiologies, showed that some special carbonate shapes and micropores are exclusive to a certain physiology. This suggests the information of iron

reducing physiology can be recorded in carbonate minerals, which may be used as a biomarker to indicate the presence of life on the early Earth.

Cerium is an important paleoredox probe, since it is the only rare earth element with an active redox chemistry at Earth surface temperatures. However, lack of details about mechanism of Ce redox and its anomalous behavior obstructs the use of Ce as a redox tracer to understand past sedimentary environments. The experimental results indicated *Roseobacter sp*. AzwK-3b, a superoxide producer, is able to oxidize Ce(III) through the superoxide pathway. On the other hand, the iron reducer *S. oneidensis MR-1* can reduce cerium(IV) directly, and uses cerium as the sole electron acceptor for anaerobic respiration. This study indicates a new biological mechanism of Ce redox.

Volcanic ash contains 1-10% FeO by weight and could be a significant contributor of Fe to fertilize oceans in the past. A 49 meter Eagle Ford core (late Cretaceous), containing 51 visualized ash beds with varying thickness, was scanned with X-ray *fluorescence* microscopy to determine burial of Fe, trace elements delivered to the sediment by sinking organic matter (Ni), and paleoredox proxies (Mo and Cr) below, in, and above ash beds. Ash beds contain much more Fe, Mo and Ni, but less Cr than interbedded black shales. This suggests that input of ash increased marine primary productivity (Ni), which in turn enhanced oxygen demand and promoted euxinia (Mo and Cr). We conclude that Fe-bearing volcanic ash fertilized the Late Cretaceous Western Interior Seaway.

ACKNOWLEDGEMENTS

First and foremost I am grateful to my committee chair, Dr. Michael Tice, for his guidance, patience and support. It has been an honor to be his Ph.D. student, and a great pleasure to work with him. I appreciate his contributions of time, ideas, and funding to this dissertation, and the many opportunities he offered to prepare me for my academic career. I would like to express my gratitude to my other committee members: Dr. Michael Pope for geologic field work training, Dr. Franco Marcantonio for geochemistry mentoring, Dr. Paul Straight for genetic experiments guidance, and for their support and guidance throughout the course of this research.

Thanks also go to my friends and colleagues and the department faculty and staff for making my time at Texas A&M University a great experience. I want to thank the Department of Geology & Geophysics and the Berg-Hughes Center for providing fellowship.

Last but not the least, I would like to thank my parents for their spiritual support and encouragement.

NOMENCLATURE

BIF	Banded Iron Formation
EDS	Energy Dispersive Spectrometer
HEPES	4-(2-hydroxylethyl)-1-piperazineethanesulfonic acid
EPS	Extracellular Polymeric Substances
HEPES	4-(2-hydroxylethyl)-1-piperazineethanesulfonic acid
IHTC	Isonicotinic acid hydrazide and 2,3,5-triphenyltetrazolium chloride
LBB	Leucoberbelin Blue
SEM	Scanning Electron Microscope
SI	Saturation Index
SOD	Superoxide Dismutase
XRD	X-ray Diffraction
XRF	X-ray *Fluorescence* Microscopy

TABLE OF CONTENTS

Page

LIST OF FIGURES

Page

Page

Page

Page

LIST OF TABLES

Page

CHAPTER I

INTRODUCTION

To detect the earliest life from the geologic record is difficult because biological evidence (biosignatures) are destroyed over time, so that complex organic molecules (e.g. DNA) are gone in 6.8 million years (Allentoft et al., 2012). Long lasting biosignatures, however, often are confused with the products of abiotic processes. Carbonaceous microfossils used to be considered the most definitive evidence of ancient life, but recent evidence suggests that similar structures may be formed through abiotic hydrothermal processes (Brasier et al., 2002). Similarly, carbon isotopic fractionation less than -15‰ is associated with enzymatic processes, but such carbon fractionation can also be produced by abiotic processes (Horita and Berndt, 1999).

Why is it a challenge to obtain an ideal biosignature completely excluding abiotic processes? That is because life is basically chemical reactions, and enzymes only speed up the chemical reaction rate but do not influence reaction direction or products. That means, in principle, that biological products may be produced abiotically as long as there is enough time. However, the appearance of complex organic materials contradicts this argument. Complex organic materials (e.g. DNA fragments), shells, and bones are produced through delicate enzymatic processes, thus they are nearly time independent. However, the earliest life forms (microorganisms) did not have fossilizable skeletons and shells. More complex organic molecules are stronger evidence of life, but unfortunately, more complex organic structures are less stabilize than simple

compounds. When dealing with the identification of life billions years ago, searching for complex organic molecules as evidence is unpromising.

Due to the lack of a “smoking gun”, the major recent approach in the identification of early life is the use of systematic tests such as the “list of criteria approach” (Buick, 1984; Schopf, 1983). The strategy of these criteria is, rather than relying on a single biosignature, to score the potential biologic structure by a bundle of tests which biological structures should pass, and labeling the high scoring candidates as “probable microfossils”. However, “probable” answers are not satisfying. A new approach or “smoking gun” needs to be explored in order to identify the earliest life.

Preserved signatures from microbial physiology in rocks could provide a new generation of evidence. On a global scale, microbial processes are a critical force for driving global geobiochemical cycling, reorganizing the distribution of trace elements (Tribovillard et al., 2006), and thus shaping the Earth’s surface throughout geologic time. On a cellular scale, bacterial physiology creates steep chemical gradients between local environments around the cell and ambient environments. Such influence is only highlighted around single cells, and can be distinguished from abiotic bulk fluids. For instance, microbial carbonates are precipitated by microbial sulfate reduction (Bosak and Newman, 2003) and cyanobacterial photosynthesis (Thompson and Ferris, 1990). In comparison to inorganically produced carbonates, microbial carbonates often have their own specific properties of shape, size, crystallinity, isotopic and trace element compositions (Weiner and Dove, 2003).

Recent research hints that bacterial physiology could be preserved as bacterial "footprints" in rock records and be a useful biosignature to identify the earliest life. For instance, bacteria cell surfaces provide a nucleation site for carbonate growth (Van Lith et al., 2003), and induces exclusive carbonate morphologies and microporosity (Dupraz et al., 2009; Warthmann et al., 2000b); Superoxide produced by microorganisms can broadly oxidize elements in seawater (Learman et al., 2011); and microbes boost ocean productivity after volcanic ash injection, thus may enhance euxinic condition in marine sediments (Duggen et al., 2010). To evaluate the potential of bacterial physiology as a biosignature, this dissertation explored how mechanisms of bacterial physiologies controlling carbonate precipitation, mediate cerium redox, and influenced the Late Cretaceous ocean productivity and sediment euxinic condition with increased input of volcanic ash.

I.1 OVERVIEW

Chapter II studies how microbial iron reduction induced carbonate nucleation and growth under different chemical compositions. *Shewanella oneidensis MR-1* was incubated anaerobically to reduce iron. Electron microprobe was used to analyze the composition of precipitated carbonate and observe the nucleation on cell surfaces. The concentrations of Fe^{2+} and *p*H were measured during iron reduction to build a geochemical precipitation model.

Chapter III presents the regulation of different iron reducing physiologies (membrane-bound enzyme, electron shuttle, and nanowires) on carbonate morphologies and micropores formation. *S. oneidensis MR-1*, *G. fermentans*, and *G. metallireducens GS-15*, representing these three different iron reducing physiologies, were incubated under identical conditions, and the scanning electron microscope (SEM) images of carbonate and micropores were analyzed to determine the differences in their morphology.

Chapter IV assesses the ability of superoxide producing bacteria to oxidize cerium (III), and tests whether metal reducing bacteria can reduce cerium(IV) directly. *Roseobacter sp*. AzwK-3b, a superoxide producer, was incubated in both agar and liquid medium containing Ce(III) to trigger the potential cerium oxidation. *S. oneidensis MR-1*, a metal reducer, was cultured anaerobically and supplied $Ce(SO_4)_2$ as the sole electron acceptor to study the mechanism of microbial cerium reduction.

Chapter V determines whether volcanic ash locally increased productivity in Cretaceous ocean, and enhanced euxinia by using trace elements as paleoproductivity

and paleoredox proxies. A 49 meter Eagle Ford Group core (late Cretaceous), containing 51 visualized ash beds with varying thickness, were scanned with X-ray *fluorescence* microscopy to examine burial of Fe, trace elements delivered to the sediment by sinking organic matter (Ni), and paleoredox proxies (Mo and Cr) below, in, and above the ash beds.

CHAPTER II[1]

PROMOTION AND NUCLEATION OF CARBONATE DURING MICROBIAL IRON REDUCTION

II.1 OVERVIEW

Iron-bearing early diagenetic carbonate cements are common in sedimentary rocks, where they are thought to be associated with microbial iron reduction. However, little is yet known about how local environments around actively iron reducing cells affect carbonate mineral precipitation rates and compositions. Precipitation experiments with the iron reducing bacterium *Shewanella oneidensis MR-1* were conducted in order to examine the potential role of cells in promoting precipitation and to explore the possible range of precipitate compositions generated in varying fluid compositions. Actively iron reducing cells induced elevated carbonate mineral saturation and nucleated precipitation on their poles. However, precipitation only occurred when calcium was present in solution, suggesting that cell surfaces lowered local ferrous iron concentrations by adsorption or intracellular iron oxide precipitation even as they locally raised *p*H. Resultant precipitates were a range of thermodynamically unstable calcium-rich siderites that would likely act as precursors to siderite, calcite, or even dolomite in nature. By modifying local *p*H, providing nucleation sites, and altering metal ion

[1] Chapter II has been published as "Promotion and nucleation of carbonate during microbial iron reduction. Zhirui Zeng and Michael M. Tice. Geobiology, 12, 362-367. Copyright (2014), John Wiley and Sons". http://onlinelibrary.wiley.com/doi/10.1111/gbi.12090/full

concentrations around cell surfaces, iron reducing microorganisms could produce a wide range of carbonate cements in natural sediments.

II.2 INTRODUCTION

Anaerobic respiration by microorganisms promotes carbonate cement precipitation (Canfield and Raiswell, 1991; Coleman, 1985; Froelich et al., 1979; Krumbein, 1978; Reid et al., 2000; Roden and Ferris, 2000; Visscher et al., 2000; Warthmann et al., 2000a; Wright, 1999), and these cements may represent a significant sink in the global carbon cycle (Schrag et al., 2013). Sulfate reduction is commonly understood to promote carbonate precipitation by reactions 2.1 and 2.2.

$$SO_4^{2-} + 2CH_2O \rightarrow HS^- + 2HCO_3^- + H^+ \quad (2.1)$$

$$Ca^{2+} + HCO_3^- \rightarrow CaCO_3 + H^+ \quad (2.2)$$

Reaction 2.1 drives reaction 2.2 by increasing the concentration of dissolved bicarbonate leading to an increased saturation index for $CaCO_3$. Sulfate reduction thus traps some remineralized organic carbon as precipitated cement in organic-rich rocks. In contrast, iron reduction (reaction 2.3) promotes carbonate precipitation by increasing the local *p*H, thus increasing the saturation index of $CaCO_3$.

$$4Fe(OH)_3 + CH_2O + 7H^+ \rightarrow 4Fe^{2+} + HCO_3^- + 10H_2O \quad (2.3)$$

Iron reducers are phylogenetically diverse and found in both the Bacteria and Archaea (Weber et al., 2006). Iron comprises 4.3% of deep marine sediments on average (Poulton and Raiswell, 2002). However, active redox cycling between oxidizers and reducers can lead to the reduction of the same iron atom many times before it is finally

sequestered in a mineral phase (Johnson et al., 2008), allowing iron reduction to account for up to 50-90% of respired organic matter in some marine sediments (Canfield et al., 1993). These factors all make iron reduction a ubiquitous and globally significant biogeochemical process (Lovley, 1991) that drives element cycling in many marine sediments (Burdige, 1993). Because seven moles of H^+ are consumed, reaction 3 could potentially drive precipitation of seven moles of $CaCO_3$ per mole of inorganic carbon produced. This suggests that iron reduction could sequester carbon released from other metabolic reactions or even act as a sedimentary sink for marine inorganic carbon, potentially in excess of the burial of organic carbon itself. The source of inorganic carbon buried and the magnitude of the authigenic carbon sink therefore depend on the specific anaerobic metabolism that drives carbonate precipitation. Identifying the source of authigenic cements and understanding the factors that control precipitation are therefore critical for evaluating the significance of diagenetic carbonate sinks to past carbon cycles.

The chemical environments in which carbonate minerals precipitate can be reflected in their compositions. A wide range of Fe/Ca ratios occur in early diagenetic carbonate cements (Curtis, 1986; Gluyas, 1984). Varying microbial iron reduction rates are thought to be largely responsible for this variation (Mortimer et al., 1997). However, microorganisms can affect carbonate precipitation in multiple ways, including acting as heterogeneous precipitation nuclei (Bosak and Newman, 2003; Dupraz et al., 2009). Under these circumstances, microbial surfaces could affect mineral composition by modifying precipitation rates, or by locally decreasing concentrations of metals, either

by adsorption or by precipitation of secondary minerals (Glasauer et al., 2002). Little is yet known about how such interactions may impact the composition of carbonate minerals precipitated during microbial iron reduction.

II.3 MATERIALS AND METHODS

The iron reducing bacterium *Shewanella oneidensis MR-1* was cultured in basal medium in an anaerobic chamber containing 88% N_2, 7% CO_2 and 5% H_2. Although *S. oneidensis MR-1* oxidizes lactate ($CH_3CHOHCOO^-$) to acetate (CH_3COO^-) rather than bicarbonate (Lovley et al., 1989), this incomplete oxidation does not significantly affect *p*H evolution under the conditions examined in these experiments. *S. oneidensis MR-1* thus provides a close model for the general iron reduction reaction occurring in sediments. The basal medium was modified from Marsili et al. (2008) by removing trace elements, 4-(2-hydroxylethyl)-1-piperazineethanesulfonic acid (HEPES), and by reducing the total phosphate concentration to prevent precipitation of iron phosphate minerals. Final medium contained 10 mM NH_4Cl, 0.1 mM $MgCl_2$, 0.1 mM KH_2PO_4, 0.5 g/L of casamino acid, 5 mM ferric hydroxide (electron acceptor), and 20 mM lactate (electron donor). Fresh ferric hydroxide was prepared with filter-sterilized $FeCl_3$ (Fu et al., 2009). 10 mM of $CaCl_2$ was added to all treatments except for calcium-free controls. Medium $[Mg^{2+}]/[Ca^{2+}]$ ratios and total $[Na_2SO_4]$ were set to bracket historical marine values (Knoll et al., 2012; Ries et al., 2008), with $[Mg^{2+}]/[Ca^{2+}]$ = 0, 5, and 10, and total $[Na_2SO_4]$ = 0, 5 and 28 mM. Factorial experiments were constructed over all treatment variables and performed with 10 replicates each. NaCl was used to equalize ionic

strength across all treatments. The basal medium and all chemical supplements were sterilized by 0.2 µm filter.

Medium with 5 mM ferric hydroxide were equilibrated in an anaerobic chamber for 3 days and titrated to *p*H 6.7–7.2. *S. oneidensis MR-1* was incubated in LB medium overnight. Cells were harvested by centrifugation, washed with basal medium, and adjusted to an optical density of 1.0 at 600 nm. 1 L of equilibrated medium was inoculated with 10 mL of washed cells. Medium, ferric hydroxide, and cells were then transferred into 96 well plates (300 µL per well) with 10 replicates for each treatment. Duplicate plates were prepared for analysis at 0, 5, 10, and 15 days. To minimize evaporation of medium from plates, the outside rows and columns of each plate were filled with nanopure water and not used for experimental treatments. Incubation took place in an anaerobic chamber at 23 °C.

Ferrous iron measurements were performed by the ferrozine assay (Viollier et al., 2000), and *p*H measurements were performed by microelectrode (Micro *p*H electrode, Fisher Scientific). All preparations and measurements except for the final spectrophotometric step of the ferrozine assay were performed in the anaerobic chamber.

Because sample volumes harvested from wells were small, large volumes (30 mL) of experimental treatments were prepared in 50 mL conical tubes under duplicate conditions and *p*H = 7.1 to produce sufficient material for mineral analysis. After 1 month incubation, samples from tubes were washed with nanopure water at least three times and dried in the anaerobic chamber. Both optical microscopy and electron microscopy were used to analyze grain morphology and grain size. Images were

acquired by a four spectrometer Cameca SX50 electron microprobe at an accelerating voltage of 15 kV and a beam current of 100 pA. Comparative and quantitative measurements were collected for all mineral grains with a Princeton Gamma Tech Imix energy dispersive spectrometer (EDS) using a thin-window detector. To distinguish iron carbonate from other iron minerals (e.g. lepidocrocite), Raman scattering spectra of selected samples were obtained with a Horiba Jobin-Yvon LabRam IR system with 632 nm laser excitation line at intervals of 2 cm^{-1} (100-2000 cm^{-1}). Bulk mineral identifications were performed on select samples from large-volume treatments using a X-ray diffraction (XRD) (Bruker D8) with Cu-*K*α radiation at an accelerating voltage of 35 kV and a filament current of 45 mA. Continuous incubation was sustained up to six months to test for changes in grain size and mineral composition. Visual MINTEQ 3.0 (Gustafsson, 2006) was used to calculate mineral saturation indices at either the beginning or end of experiments (equation 2.4).

$$\mathrm{SI} = \log[\mathrm{Me}^{2+}][\mathrm{CO}_3^{2-}] - \log K_{\mathrm{sp}} \qquad (2.4)$$

Here, $[Me^{2+}]$ is the calculated free concentration of Ca^{2+} or Fe^{2+} and K_{sp} is the solubility product. The logK_{sp} is -8.3 for calcite and -10.6 for siderite.

II.4 RESULTS

S. oneidensis MR-1 iron reduction promoted carbonate mineral precipitation in all calcium-containing treatments (Fig. 2.1). No precipitation occurred in calcium-free treatments or in abiotic controls during one-month-long incubations. Bulk solution *p*H rose by approximately 0.2 log units (standard error < 0.01 log units) during 15 day

incubation. EDS (Fig. 2.2) and XRD (Fig. 2.3) analysis showed that resultant carbonate minerals were calcium-rich siderite. Typical carbonate grains were spherical (Fig. 2.1A-I). In 15 day incubations, precipitation was nucleated on bacterial poles (Fig. 2.4 A-B). During extended incubations for two or more months, large spherical carbonate with bulk compositions of approximately $Ca_{0.4}Fe_{0.6}CO_3$ (Fig 2.4C and Table 2.1) was formed. Although high $[Mg^{2+}]/[Ca^{2+}]$ ratios slowed or partially inhibited carbonate precipitation, producing fewer and smaller carbonate grains (Fig. 2.5) and changing mineral compositions (Table 2.1), they did not alter grain morphologies (Fig. 2.1). Sulfate did not affect mineral composition or grain morphology at any concentration (Fig. 2.5), but it mitigated the inhibitory effect of high $[Mg^{2+}]/[Ca^{2+}]$ on carbonate precipitation rates (Fig. 2.6).

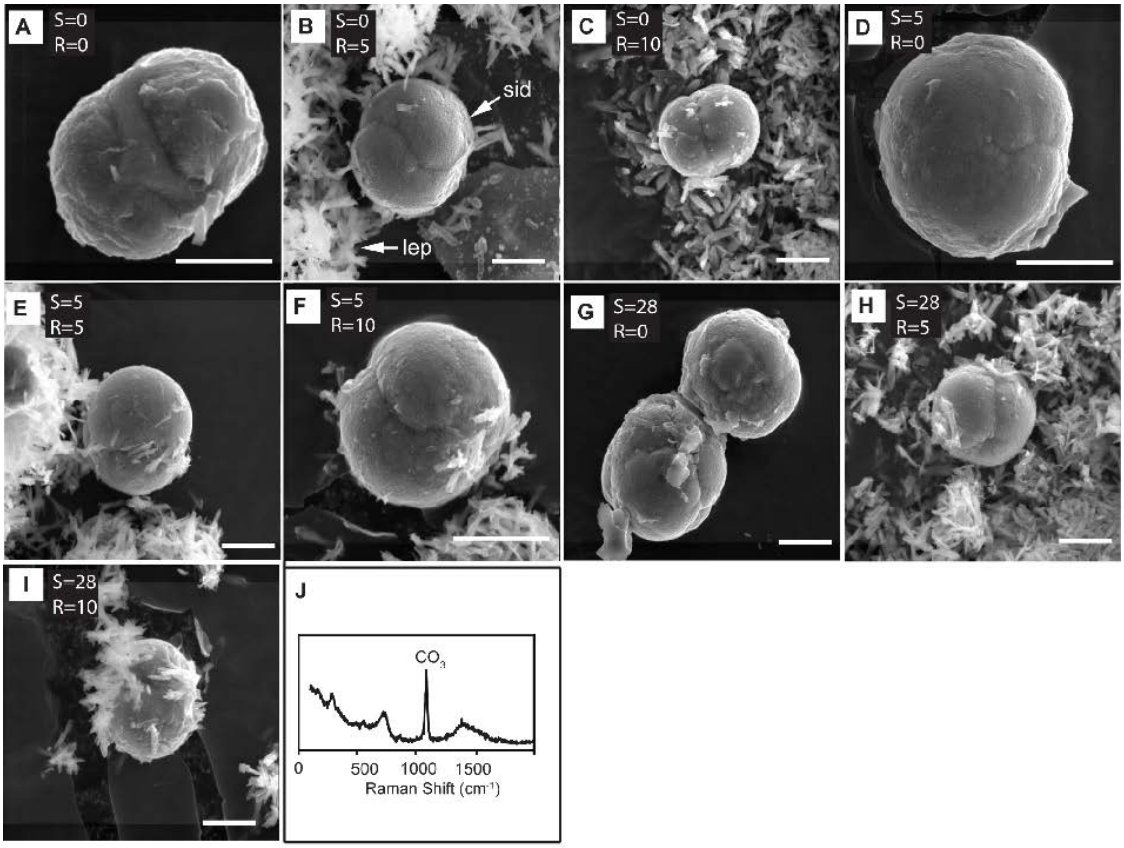

Figure 2.1. (A-I) Carbonate minerals precipitated during one-month-long iron reduction experiments with treatments noted. S = concentration of sulfate, R = ratio of $[Mg^{2+}]/[Ca^{2+}]$, sid = siderite, and lep = lepidocrocite. Scale bars are 5 µm. (J) Raman analysis of spherical grain.

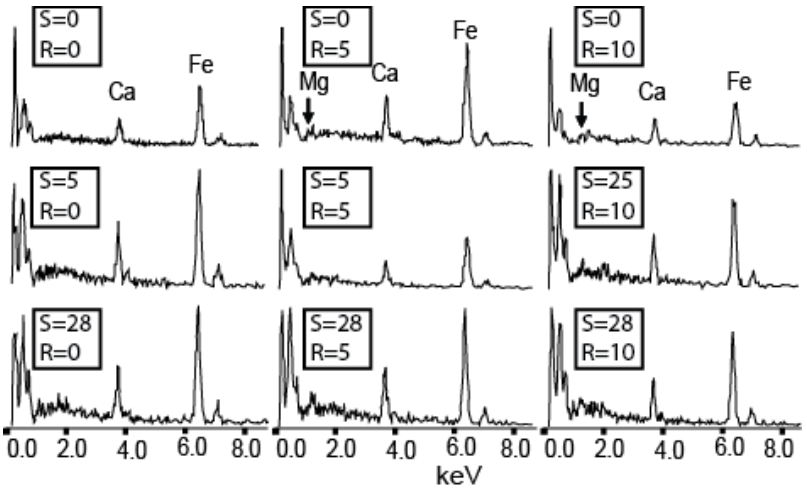

Figure 2.2. EDS analysis of carbonate minerals from Fig. 2.1. Treatments indicated as in Fig. 2.1.

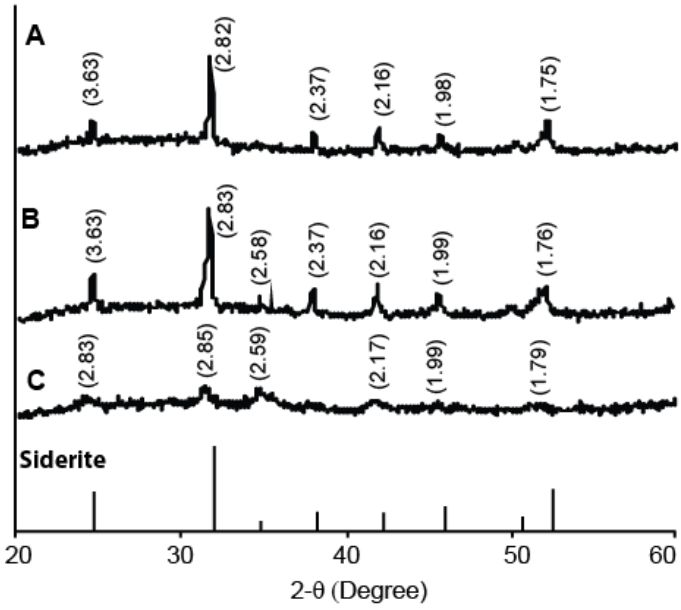

Figure 2.3. XRD analysis of selected samples precipitated during one-month-long iron reduction experiments. (A) $[SO_4^{2-}] = 0$ mM, $[Mg^{2+}]/[Ca^{2+}] = 0$. (B) $[SO_4^{2-}] = 0$ mM, $[Mg^{2+}]/[Ca^{2+}] = 5$. (C) $[SO_4^{2-}] = 0$ mM, $[Mg^{2+}]/[Ca^{2+}] = 10$.

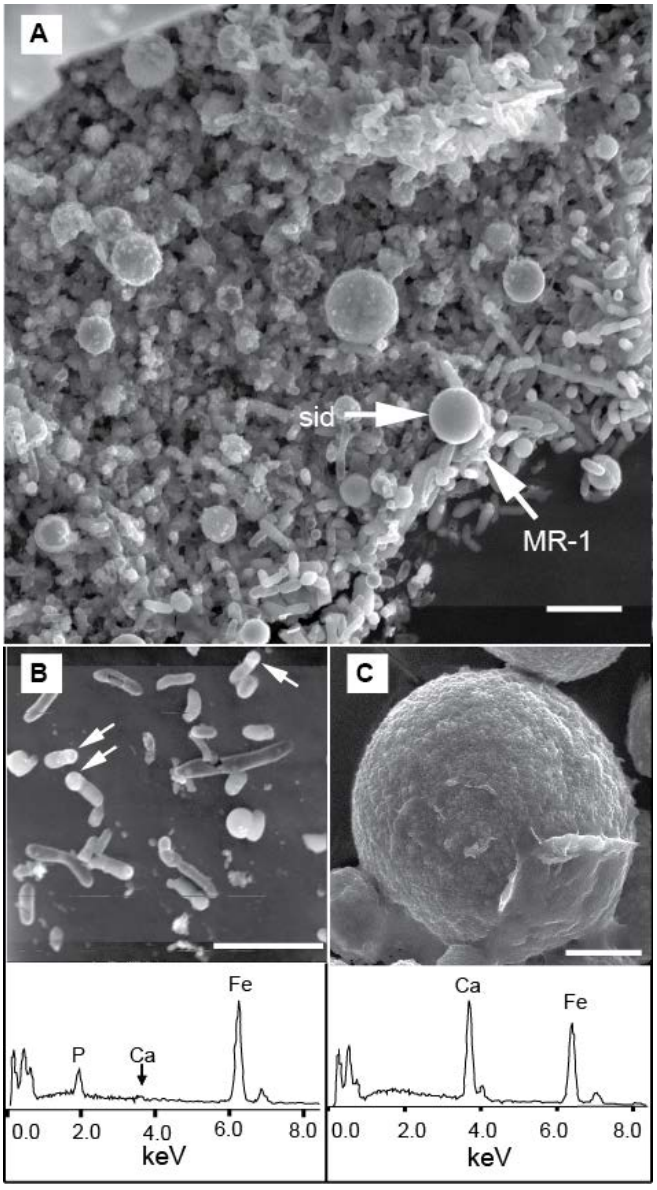

Figure 2.4. (A) Small spherical carbonate formed close to bacteria cells during early iron reduction (15 days). sid = siderite, and MR-1 = bacteria. (B) Poles of bacteria cell were coated by minerals (arrows) in 15 day incubations. EDS analyses of mineral-free surfaces of triple-washed bacteria show abundant iron and little to no calcium. (C) Long term incubation (3 months) increased siderite grain size and calcium content ($Ca_{0.4}Fe_{0.6}CO_3$). All scale bars are 5 μm.

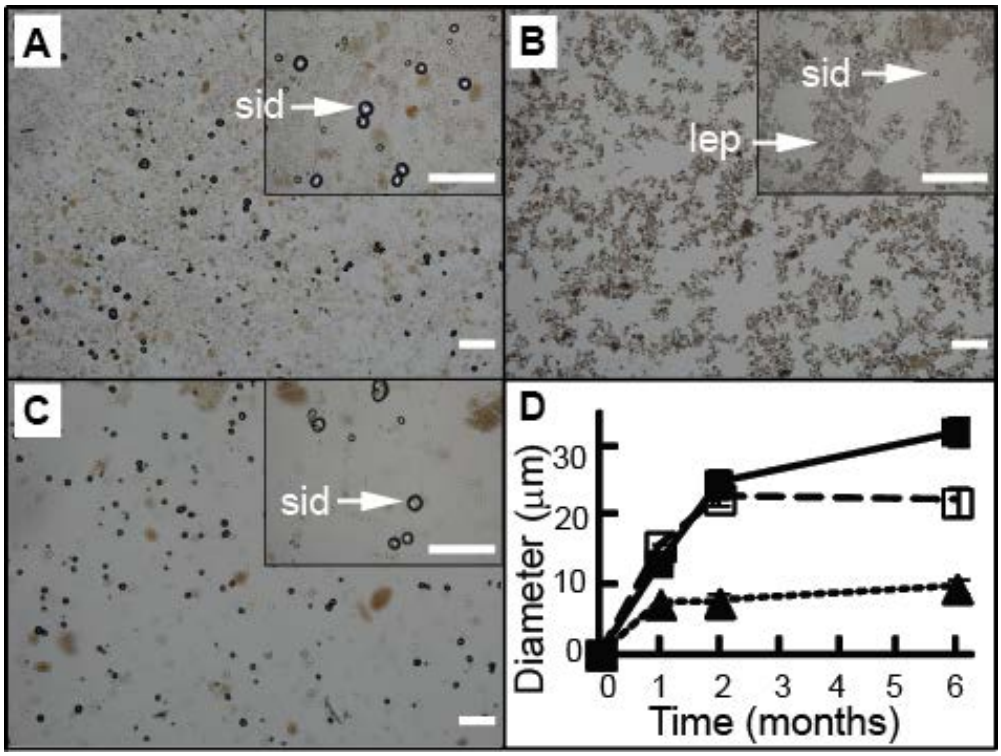

Figure 2.5. High $[Mg^{2+}]/[Ca^{2+}]$ ratio inhibited carbonate precipitation but sulfate did not affect carbonate precipitation. (A) $[SO_4^{2-}]$ = 0 mM, $[Mg^{2+}]/[Ca^{2+}]$ = 0. (B) $[SO_4^{2-}]$ = 0 mM, $[Mg^{2+}]/[Ca^{2+}]$ = 10. (C) $[SO_4^{2-}]$ = 28 mM, $[Mg^{2+}]/[Ca^{2+}]$ = 0. sid = siderite; lep = lepidocrocite. Scale bars are 100 μm. (D) Growth of grains with respect to incubation time. Solid square is $[SO_4^{2-}]$ = 0 mM, $[Mg^{2+}]/[Ca^{2+}]$ = 0, open square is $[SO_4^{2-}]$ = 28 mM, $[Mg^{2+}]/[Ca^{2+}]$ = 0 and solid triangle is $[SO_4^{2-}]$ = 0 mM, $[Mg^{2+}]/[Ca^{2+}]$ = 10.

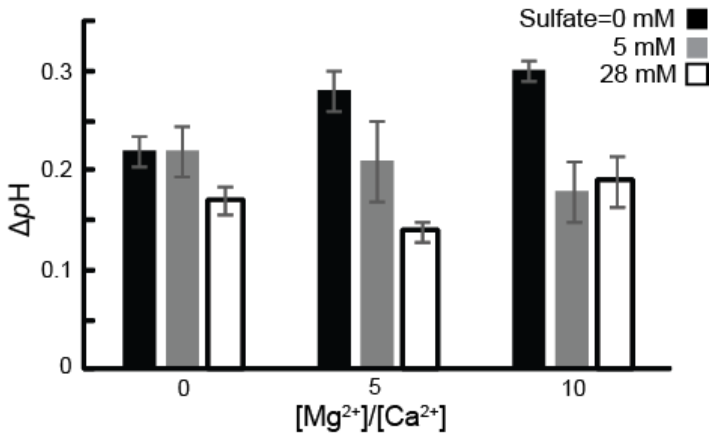

Figure 2.6. The effect of sulfate on medium *p*H buffering by carbonate precipitation. Δ*p*H was used to proxy for the amount of precipitated carbonate, where Δ*p*H = *p*H(after iron reduction) - *p*H(before iron reduction).

Table 2.1. High $[Mg^{2+}]/[Ca^{2+}]$ and long incubation increased calcium content in siderite.

$([Mg^{2+}]/[Ca^{2+}])_{solution}$	Mg_{solid} (mol %)	Ca_{solid} (mol %)	Fe_{solid} (mol %)	$(Mg/Ca)_{solid}$	$(Ca/Fe)_{solid}$	Mineral Formula
0*	0	16	84	0	0.19	$Ca_{0.16}Fe_{0.84}CO_3$
5*	5	17	78	0.21	0.22	$Ca_{0.17}Mg_{0.05}Fe_{0.78}CO_3$
10*	6	20	74	0.28	0.27	$Ca_{0.2}Mg_{0.06}Fe_{0.74}CO_3$
0†	0	40	60	0	0.67	$Ca_{0.4}Fe_{0.6}CO_3$

*One month incubation.
†Three month incubation.

II.5 DISCUSSION

II.5.1 Nucleation of Carbonate Minerals

Calcium in the growth medium was required for precipitation of any carbonate mineral despite extreme supersaturation of all experimental solutions with respect to siderite at completion of active iron reduction (siderite saturation indices of ~150).

Indeed, resultant carbonate precipitates were surprisingly enriched in calcium given the relatively low calcite saturation index achieved (<5). Cell walls are negatively charged at circum-neutral *p*H due to the presence of carboxylate ($RCOO^-$) and phosphate (RPO_4^{2-}) functional groups (Jiang et al., 2004). Differential adsorption of Ca^{2+} and Fe^{2+} to these functional groups likely explains the calcium requirement for precipitation. In general, the hard acid Ca^{2+} is expected to associate strongly with H_2O, a stronger base than either $RCOO^-$ or RPO_4^{2-}. Fe^{2+} is only a transitional acid, and will adsorb to $RCOO^-$ or RPO_4^{2-} more effectively than Ca^{2+}. This prediction of Hard Soft Acid Base Theory is consistent with observed stability constants for Ca^{2+} and Fe^{2+} complexes with chelators having carboxylate or phosphate functional groups: Fe^{2+} universally forms stronger complexes (Werner and James, 1996). Fe^{2+} adsorption to cell surfaces would then locally lower siderite saturation, but local Ca^{2+} concentrations would not be as strongly affected. Moreover, some iron reducing bacteria precipitate iron oxide within cells (Glasauer et al., 2002). Although not directly observed in this study by microprobe or Raman microspectroscopy, even small amounts of intracellular iron oxides could have significantly lowered iron concentrations near cell walls. EDS analyses of cell surfaces free of visible mineral precipitates showed abundant of iron, but calcium was at or below detection limits (Fig. 2.4B), suggesting that iron preferentially associated with cells by one or both of these mechanisms (i.e. adsorption or intracellular precipitation). Iron reduction at the cell wall would locally increase *p*H, thus primarily promoting the precipitation of an early calcium-rich carbonate coating on cell surfaces. This initial

coating would cover nearby adsorption sites for Fe^{2+}, allowing subsequent precipitation of calcium-rich siderite on the initial carbonate seed.

Magnesium inhibition of calcium carbonate precipitation by formation of hydrated magnesium ion complexes (e.g. $Mg(H_2O)_6^{2+}$) and elevation of the dehydration energy around carbonate surfaces has been well studied (Fernandez-Diaz et al., 1996; Richard, 1978). Consistent with those previous results, magnesium slowed both carbonate nucleation and precipitation in this study (Fig. 2.5). If initial seeds are calcium-rich, then inhibition by magnesium could also result from competitive poisoning of surface sites for calcium (Morse et al., 1997; Richard, 1983). High $[Mg^{2+}]/[Ca^{2+}]$ ratios did not affect iron reduction rates and are therefore unlikely to have inhibited carbonate precipitation by lowering mineral saturation (Fig. 2.7).

Slowing of carbonate precipitation relative to diffusion of Fe^{2+} away from sites of precipitation around bacterial surfaces could also explain observed effects of high $[Mg^{2+}]/[Ca^{2+}]$ ratios on mineral compositions (Table 2.1). In particular, because Mg^{2+} slowed overall precipitation rates, local $[Fe^{2+}]/[Ca^{2+}]$ ratios would have decreased, which would have increased the calcium content in resultant siderite (Romanek et al., 2009).

Sulfate had little to no effect on carbonate precipitation in treatments with $[Mg^{2+}]/[Ca^{2+}] = 0$ (Fig. 2.5). However, sulfate may partially relieve inhibition of precipitation by magnesium through formation of the $MgSO_4$ complex, thus lowering the free magnesium concentration. Consistent with this expectation, treatments including both sulfate and magnesium increased *p*H during iron reduction less than those

containing only magnesium (Fig 2.6), implying that they were more strongly buffered by carbonate mineral precipitation.

II.5.2 Precipitation Kinetics

Models of the evolution of experimental solution compositions were constructed to understand the kinetics of carbonate precipitation (Fig. 2.8 and Appendix). All effective equilibrium constants were set to be consistent with terminal fluid compositions as modeled by MINTEQ. Models assumed carbonate equilibrium with the atmosphere of the anaerobic chamber. Because carbonate precipitation was not observed in calcium-free controls, carbonate precipitation was modeled as a function of calcite saturation index. Fe/Ca ratios in precipitates were modeled as proportional to $[Fe^{2+}]/[Ca^{2+}]$ in solution, with the constant of proportionality adjusted to match final precipitate compositions to representative experimental compositions. Specific models used to analyze results differed in how $[Ca^{2+}]$ was allowed to evolve.

No Precipitation Model. In this model, no carbonate mineral precipitation was allowed, i.e. $d[Ca^{2+}]/dx = 0$, where x is the total amount of iron reduced. This uniquely sets the evolution of the system with no tunable parameters.

Critical Supersaturation Model. In this model, no carbonate precipitation was allowed until $[Ca^{2+}][CO_3^{2-}] = \Omega_c K_{sat}$, where K_{sat} is the calcite solubility product constant and Ω_c is the critical saturation index. Ω_c was allowed to vary to fit data generated during experiments.

Power Law Model. In this model, carbonate precipitation kinetics were explicitly modeled by Equation 2.5 (Morse, 1978):

$$-\frac{d[Ca^{2+}]}{dt} = r(\Omega - 1)^n, \quad (2.5)$$

where r and n are constants and $\Omega = [Ca^{2+}][CO_3^{2-}]/K_{sat}$. In order to model reaction progress as a function of time rather than total iron concentration, measured iron concentration time series were fit to logistic curves to estimate instantaneous rates of change. Model results did not depend critically on n for $n > 1$, so reported analyses assume $n = 3$ (Mucci and Morse, 1983). r was varied to fit experimental data.

Nucleation Limitation Model. In this model, carbonate precipitation was assumed to follow a power law dependence on saturation as in equation 2.5. However, this model also required that precipitation occur on new cell surfaces. Assuming that the number of new cell surfaces is proportional to the rate of iron reduction yields the following relationship:

$$-\frac{d[Ca^{2+}]}{dt} = r'(\Omega - 1)^n \frac{dx}{dt}. \quad (2.6)$$

Calcium-free treatment ($[Ca^{2+}] = 0$) were well-described by the No Precipitation Model despite the lack of any tunable parameters (Fig. 2.8A), consistent with the lack of carbonate precipitates in this treatment. In experiments with added calcium, measured *p*H was always less than that predicted by the No Precipitation Model (Fig. 2.8B), suggesting that *p*H was partially buffered by carbonate precipitation, consistent with the presence of calcium-rich siderite in all such treatments. The Critical Supersaturation Model did not fit data for calcium-containing treatments for any single critical saturation index (Fig. 2.8B), and the Power Law Model overestimated precipitation rates when iron reduction was complete (Fig. 2.8C). The Nucleation Limitation Model provided the best

fits (Fig. 2.8D), suggesting that carbonate precipitation was most rapid when high saturation indices were combined with abundant fresh bacterial surfaces to act as heterogeneous precipitation nuclei. This dual dependence was seen most clearly when the ferric hydroxide substrate was nearly consumed and carbonate saturation indices were greatest but cell replication had slowed. At this point, precipitation was slower than predicted by carbonate saturation alone, resulting in *p*H buffering comparable to that predicted by the No Precipitation Model. These results are consistent with microscopic observations of early precipitates nucleated from cell poles (Fig. 2.4B).

II.5.3 Carbonate Mineral Compositions

These experiments produced siderite with up to 20 mol% Ca, but even more calcium-rich precipitates should be possible in nature if iron reduction is slower relative to diffusive loss of Fe^{2+}. This hypothesis is supported by long-term (three months) incubation results in which $Ca_{0.4}Fe_{0.6}CO_3$ was precipitated. After iron reduction was nearly complete at one month, extreme local iron concentrations were not sustained around bacteria or existing mineral grains, causing the composition of the bulk solution to dominate precipitation. This situation is probably most similar to natural systems in which iron reduction occurs in highly permeable sediments. Thus, early diagenetic iron-rich carbonate cements are likely to be less common in sandstones than in mudstones.

Sulfate reduction could also potentially increase the Ca/Fe ratio in carbonate precipitates. This is because sulfate reduction produces sulfide which provides a diffusive sink for Fe^{2+} at the base of the iron reducing zone through precipitation of low-solubility iron sulfides. The formation of pyrite thus decreases the local $[Fe^{2+}]/[Ca^{2+}]$

ratio, ultimately increasing the calcium content in precipitates formed at the base of the iron reducing zone (Fig. 2.9). This effect would be more important in Phanerozoic marine sediments than in freshwater sediments or Archean and Proterozoic sediments due to lower early marine sulfate concentrations (Canfield et al., 2007; Fike et al., 2006; Habicht et al., 2002).

Siderite with calcium content >15 mol% is rare to absent in nature (Romanek et al., 2009). Because most of the minerals observed in this study are metastable at low temperature (Woods and Garrels, 1992), it is likely that similar carbonates would recrystallize to form calcite and siderite in natural sediments or partially equilibrate with evolving pore fluids to form new minerals during later diagenesis (Fig. 2.10). This prediction is supported by production of precipitates close in composition to ankerite during long-term incubations. It is also consistent with observations of a range of siderite and ankerite compositions in the Early Cretaceous Kuparuk Formation (South Africa) which have been suggested to have formed during diagenesis during and after iron reduction (Mozley and Carothers, 1992).

Calcium-rich siderite also could serve as a precursor to dolomite through substitution of magnesium for iron (Nash and Pittman, 1975). For instance, late-stage ferroan dolomite is formed during magnesium release resulting from smectite conversion to illite in argillaceous mudstones (McHargue and Price, 1982). Thus, microbial iron reduction could contribute to dolomite formation by providing a metastable precursor far from equilibrium with diagenetic pore fluids.

Microbial iron reduction is likely to have been significant during the early diagenesis of banded iron formations (Konhauser et al., 2005; Nealson and Myers, 1990; Walker, 1984). Banded iron formation (BIF) precursors were probably admixtures of highly reactive fine-grained ferric hydroxides and organic matter deposited as finely laminated sediments in low energy environments (Walsh and Lowe, 1999). Iron reduction would have rapid relative to diffusion of iron out of and calcium into sedimentary pores under these conditions, resulting in early carbonate precipitates that were closer to high-calcium siderite than ankerite. This effect would have been amplified by the lack of significant sulfate reduction in BIF precursor sediments. This may explain the prevalence of siderite relative to calcite and ferroan dolomite as accessory minerals in BIF (Klein and Beukes, 1993). Less common dolomite may reflect extended diffusive exchange of pore fluids with the water column following consumption of organic matter by iron reducers in more slowly cemented sediments. $MgCO_3$ contents in BIF siderite of up to 25% (Klein and Beukes, 1989) are not predicted by the experimental results of this study and may be the result of late-stage diagenesis.

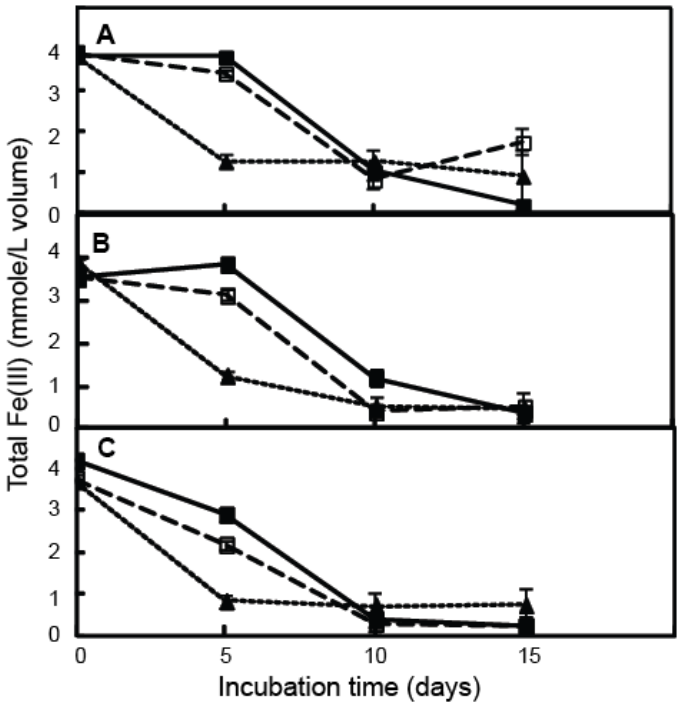

Figure 2.7. The effects of $[Mg^{2+}]/[Ca^{2+}]$ ratios and sulfate concentrations on *S. oneidensis MR-1* iron reduction rate. (A) $[SO_4^{2-}]$ = 0 mM; (B) $[SO_4^{2-}]$ = 5 mM; (C) $[SO_4^{2-}]$ = 28 mM. Solid square represents $[Mg^{2+}]/[Ca^{2+}]$ = 0, open square represents $[Mg^{2+}]/[Ca^{2+}]$ = 5, and solid triangle represents $[Mg^{2+}]/[Ca^{2+}]$ = 10.

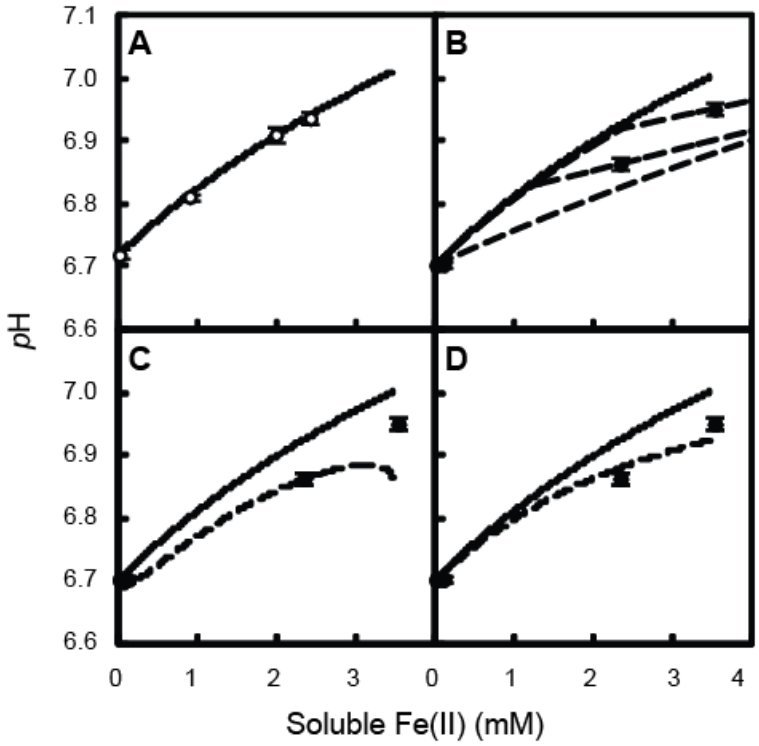

Figure 2.8. Reaction progress and model fits. (A) No Precipitation Model (solid line) fits calcium-free treatment data (open square). (B) Critical Supersaturation Model (dashed lines) does not fit data points for calcium supplement treatments for any single critical saturation index (Ω_c). (C) Power Law Model (dashed line) overestimated carbonate precipitation when iron reduction was complete. (D) Nucleation Limitation Model (dashed line) fits experimental data most closely.

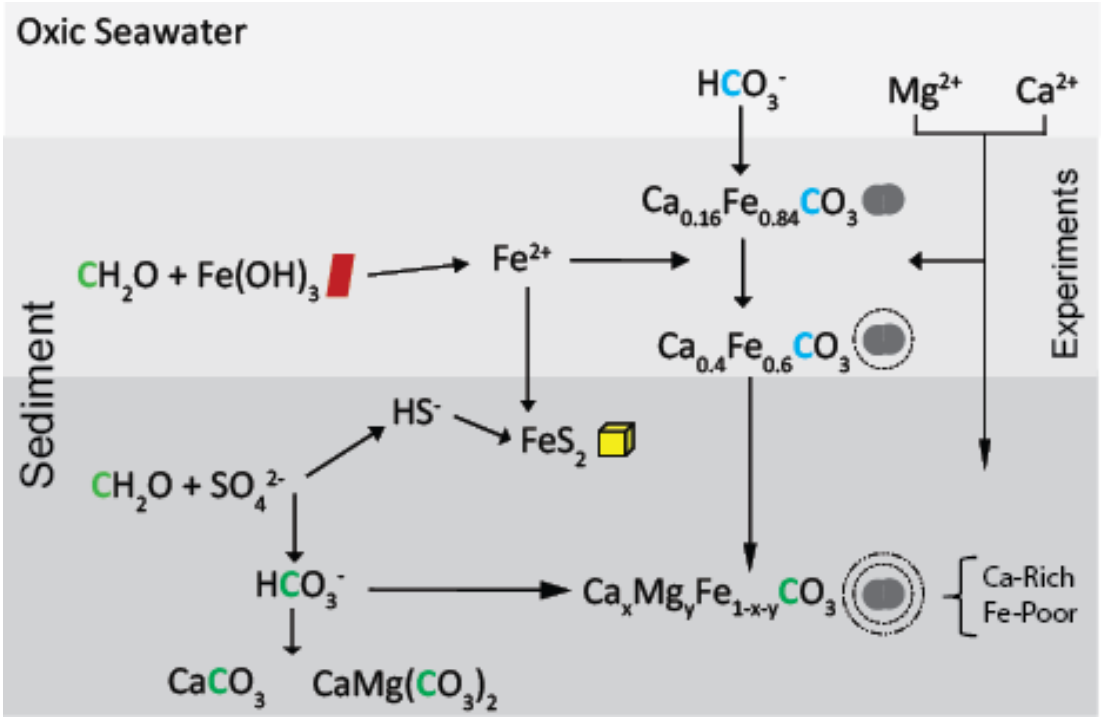

Figure 2.9. Schematic diagram illustrating a hypothetical carbonate diagenetic sequence in Phanerozoic marine sediments. Microbial iron reduction produces high calcium siderite, and the main source of carbon is bicarbonate from seawater. Sulfate reduction lower in the sediment column depletes soluble Fe^{2+} by forming iron sulfides and promotes carbonate precipitation by increasing bicarbonate concentration. Carbonate minerals become more calcium- and magnesium-rich; new carbonate comes from the oxidation of organic matter.

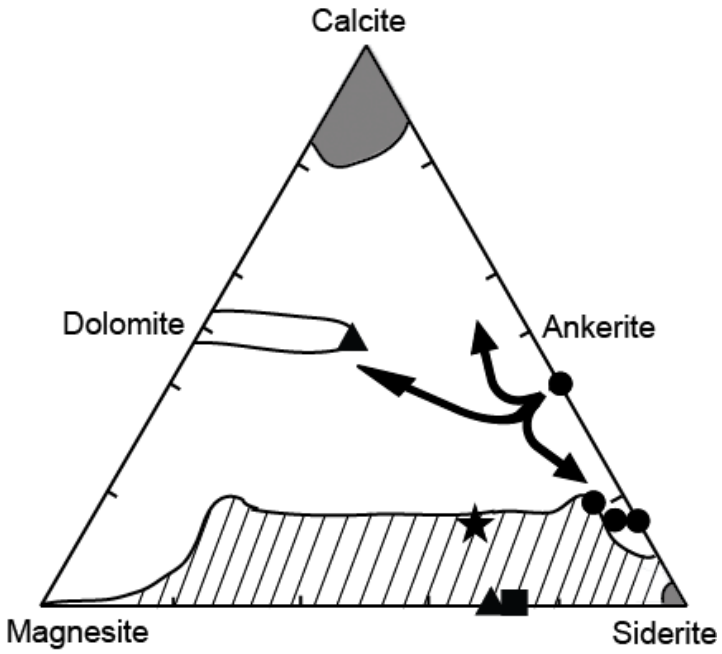

Figure 2.10. Siderite precipitated in this study compared to Fe-Mg-Ca carbonate cements in nature. Filled circles represent siderite produced in this study. Hatched-line field (Romanek et al., 2009), gray field (Pye et al., 1990) and open field (Webb et al., 2004) represent natural Fe-Mg-Ca carbonate minerals. Average carbonate mineral compositions for Kuruman iron formation (Klein and Beukes, 1993), Griquatown iron formation (Klein and Beukes, 1989), and Mendon Formation (Lowe, 1999) indicated by triangle, stars, and square, respectively. Arrows indicate hypothesized compositional evolution of high-calcium precipitates during later diagenesis.

II.6 CONCLUSIONS

Microbial iron reduction promoted precipitation of spherical calcium-rich siderite grains. Actively metabolizing cells locally raised *p*H and provided essential nucleation sites for carbonate precipitation. Precipitation only occurred when calcium was present

in solution, possibly due to local adsorption of iron on cell walls or intracellular precipitation of iron oxides. High $[Mg^{2+}]/[Ca^{2+}]$ ratios inhibited carbonate precipitation and changed mineral compositions, but did not alter carbonate morphology. Extended incubations to three months altered carbonate compositions from $Ca_{0.16}Fe_{0.84}CO_3$ to $Ca_{0.4}Fe_{0.6}CO_3$. Because most mineral compositions observed are metastable at low temperature, they could act as precursors to calcite, siderite and dolomite. By modifying local *p*H, providing nucleation sites, and altering metal ions (e.g. Ca^{2+} and Fe^{2+}) composition around cell surfaces, iron reducing microorganisms could thus produce a wide range of carbonate cements in natural sediments, including some with relatively low iron content. Microbial iron reduction may therefore play a significant but largely hidden role in the sedimentary authigenic inorganic carbon sink.

CHAPTER III

ELECTRON TRANSFER STRATEGIES REGULATE CARBONATE MINERAL AND MICROPORE FORMATION

III.1 OVERVIEW

Iron reducing bacteria apply diverse physiologies (membrane bound enzymes, soluble electron shuttles, and nanowires) to transfer electrons to insoluble iron oxide minerals, and thus may create a variety of physicochemical microenvironments in which mineral dissolution and precipitation can occur. This diversity has the potential to create mineral biosignatures recording the mechanisms by which iron reducing bacteria transferred electrons to their insoluble substrates. *S. oneidensis MR-1*, *G. fermentans*, and *G. metallireducens GS-15*, representing three different iron reducing physiologies, were incubated to reduce iron to evaluate their influence on carbonate and micropore formation. The combination of iron reduction rate and the relative distance of iron reduction from the cell wall controlled the level of local carbonate saturation and thus determined the morphology of precipitated carbonate minerals (rhombohedral or spherical). Long chains of fused spherical carbonate grains were produced during iron reduction by *G. fermentans* because the non-motile bacteria produced an extracellular electron shuttle (riboflavin) that tended to concentrate ferrihydrite reductive dissolution around local colonies, creating deep tunnels in which carbonate precipitation occurred. Iron reducing physiologies also produced distinctive micropores in both carbonate and (oxy)hydroxide minerals, thus producing suites of features that could potentially serve as

biosignatures recording information about the sizes, shapes, and physiologies of iron reducing organisms.

III.2 INTRODUCTION

Early diagenetic carbonate can be induced by microbial iron reduction (Mortimer et al., 1997; Schrag et al., 2013; Zeng and Tice, 2014) and perhaps sulfate reduction (Meister, 2013) in sediments; however, it is a challenge to distinguish biologically-induced carbonate from abiotically produced carbonate. The biofilm and extracellular polymeric substances (EPS) produced by bacteria play critical roles in carbonate precipitation by creating unique physicochemical microenvironment and providing templates for carbonate nucleation (Dupraz et al., 2009; Falini et al., 2000). The iron reducing bacterium *Shewanella oneidensis MR-1* induces carbonate precipitation by providing a nucleation site on their cell surfaces, which may magnify the biological influence on carbonate due to the close interaction between carbonate and cell surfaces (Zeng and Tice, 2014). Other iron reducing physiologies (electron transfer strategies) may also influence carbonate growth in distinctive ways by locally modifying the distributions of Fe^{2+}, H^{+}, and HCO_3^{-}.

Unlike sulfate reducing bacteria, which only use membrane-bound enzymes to reduce soluble sulfate (Ramos et al., 2012), iron reducing bacteria have evolved multiple physiologies to transfer electrons to insoluble iron minerals, including membrane-bound reductases, nanowires, and soluble electron shuttles (Weber et al., 2006). *Shewanella oneidensis MR-1* uses both outer membrane-bound proteins (e.g. OmcA and OmcB) and

soluble electron shuttles (flavins) to reduce iron minerals (Gescher et al., 2008; Xiong et al., 2006), with approximately 70-75% of electron transfer typically carried out by shuttle (Marsili, et al., 2008; Jiang, et al., 2010; Kotlowski and Gralnick, 2013). *Geobacter metallireducens GS-15* forms proteinaceous pili, or nanowires, that function as electrical conduits to transfer electrons to iron minerals (Reguera et al., 2005; Tremblay et al., 2012). In this strategy, nanowires act as a bridge between the bacterial cell and iron minerals, extending access to iron minerals beyond the reach of the cell membrane. *Geothrix fermentans* exports soluble compounds that act as electron shuttles to mediate iron reduction (Nevin and Lovley, 2002), allowing this strain to reduce iron minerals at a distance and without physical contact with minerals.

Iron reducing physiologies provide an ideal platform for investigating the role of physiological diversity in producing distinct biosignatures during biomineralization. Therefore, dissimilatory iron reducers *S. oneidensis MR-1*, *G. fermentans*, and *G. metallireducens GS-15*, representing three different iron reducing physiologies, were used to constrain the effect of iron reducing physiologies on carbonate and micropore formation.

III.3 MATERIALS AND METHODS

S. oneidensis MR-1, *G. fermentans*, *G. metallireducens GS-15* were incubated in medium containing 10 mM NH_4Cl, 0.1 mM $MgCl_2$, 0.1 mM KH_2PO_4, 0.5 g/L of casamino acid, 5 mM ferric hydroxide (electron acceptor), and 20 mM lactate (electron donor). Fresh ferric hydroxide was prepared with filter-sterilized $FeCl_3$ (Fu et al., 2009).

Medium was titrated in an anaerobic chamber (88% N_2, 7% CO_2 and 5% H_2) and adjusted to desired *p*H values (6.3-8.2) with NaOH, then amended with 1M of sterile $CaCl_2$ to obtain Ca^{2+} concentrations of 0.6-100 mM. NaCl was used to equalize ionic strength across all treatments. Aliquots of 50 mL final medium solution were inoculated with bacteria and transferred into 100 mL serum bottles. Sealed bottles were incubated in an anaerobic chamber at room temperature (23° C) for one month (*S. oneidensis*) or two months (*G. fermentans* and *G. metallireducens* in *p*H>7 media) until carbonate was formed.

During incubation, ferrous iron was measured by the ferrozine assay (Viollier et al., 2000), and *p*H was measured by microelectrode (Micro *p*H electrode, Fisher Scientific). To analyze precipitated minerals, cultured samples were washed with nanopure water three times and dried in the anaerobic chamber. Mineral products were imaged by optical microscopy and electron microscopy (Cameca SX50 electron microprobe with an accelerating voltage of 15 kV and a beam current of 100 pA).

Mineral products were identified with a Princeton Gamma Tech Imix energy dispersive spectrometer (EDS) and a Raman microspectrometer (Horiba). All spectra used for EDS quantitative analysis of carbonate crystals were acquired at an accelerating voltage of 15 kV, a beam current of 3 nA, and an acquisition time of 20 seconds. The raw count, background-corrected peak height data measured from the spectra were processed for matrix corrections through R.A Waldo's GMRfilm program (Waldo et al., 1993) using the bulk analysis option. Because our previous study showed that carbonate was the dominant precipitate during microbial iron reduction under these experimental

conditions (Zeng and Tice, 2014), only selected grains were checked with Raman spectrum microscopy for the presence of carbonate bonds in this study.

The initial saturation index (SI) of $CaCO_3$ in each culture medium prior to iron reduction was calculated using Visual MINTEQ 3.0 (Gustafsson, 2006) following equation 3.1:

$$\mathrm{SI} = [\mathrm{Ca}^{2+}][\mathrm{CO}_3^{2-}]/K_{\mathrm{sp}} \quad (3.1)$$

where $K_{sp} = 10^{-8.3}$ is the calcite solubility product.

III.4 RESULTS

III.4.1 Saturation

The morphologies (Fig. 3.1) and compositions of carbonate minerals produced during *S. oneidensis MR-1* iron reduction were highly correlated with initial saturation indices of calcite (Fig. 3.2). Rhombic grains were formed when initial SI was less than 11 (Fig. 3.1A), while spherical grains were produced when initial SI was greater than 11 (Fig. 3.1C). Grains with morphologies intermediate between these two extremes (Fig. 3.1B) occur in cultures with relative high *p*H and low Ca^{2+} concentrations (Fig. 3.2). The calcium contents of carbonates were correlated with initial calcite saturation (Fig. 3.2). In the absence of Ca^{2+}, siderite was not precipitated unless the initial *p*H was greater than 7.6.

III.4.2 Carbonate Morphologies and Micropores

All three types of physiologies formed rhombic carbonate grains under low initial calcite saturation (Fig. 3.2). However, only *S. oneidensis* and *G. fermentans* cultures

(membrane-bound enzyme and electron shuttle physiologies, respectively) formed spherical carbonate grains at greater initial saturation. Different cultures sometimes precipitated carbonate grains having different morphologies under identical initial culture conditions (Table 3.1). For instance, *S. oneidensis MR-1* (membrane-bound enzymes) produced spherical grains at $[Ca^{2+}]$=10 mM, *p*H=7.15, and SI ≈ 22 (Fig. 3.2), while *G. fermentans* cultures (electron shuttles) formed rhombic grains under the same conditions (Fig. 3.2), and *G. metallireducens GS-15* (nanowires) did not precipitate carbonate at all (Fig. 3.2). Moreover, carbonate grains formed by *G. fermentans* tended to form long chains at high saturation (e. g. $[Ca^{2+}]$=10 mM and *p*H=7.4; Fig. 3.3A).

Different cultures also produced distinctive micropores in carbonate and iron oxide minerals. *S. oneidensis MR-1* cells attached to iron minerals, where they reduced and dissolved material directly from the solid surfaces, thus forming cell-shaped micropores on iron mineral surfaces (Fig. 3.4A). In contrast, *G. metallireducens GS-15* cultures formed cavities much larger than individual bacterial cells (2.5-3.4 μm in diameter) in ferric hydroxides which were subsequently filled with precipitated carbonate grains (Fig. 3.4B). *G. fermentans* cultures did not produce pores in ferric hydroxides as did *S. oneidensis MR-1* and *G. metallireducens GS-15* cultures (Fig. 3.4C). However, cell-shaped micropores in precipitated carbonate were observed (Fig. 3.3B) having sizes slightly larger than *G. fermentans* cells (Fig. 3.3D).

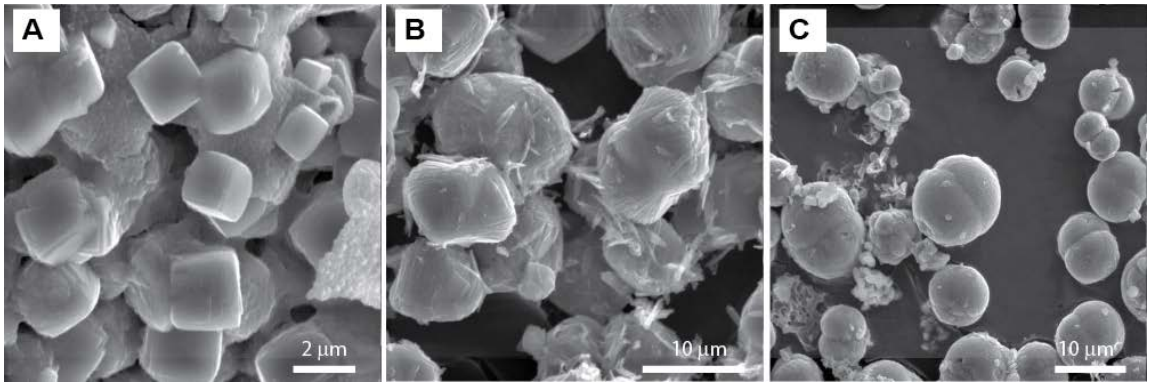

Figure 3.1. Carbonate grains were gradually transformed from rhombohedral to spherical morphology as SI increase in *S. oneidensis MR-1* iron reduction. (A) Ca^{2+}=10 mM, *p*H=6.7, SI=2. (B) Ca^{2+}=2 mM, *p*H=7.4, SI=8. (C) Ca^{2+}=10 mM, *p*H=7.2, SI=16.

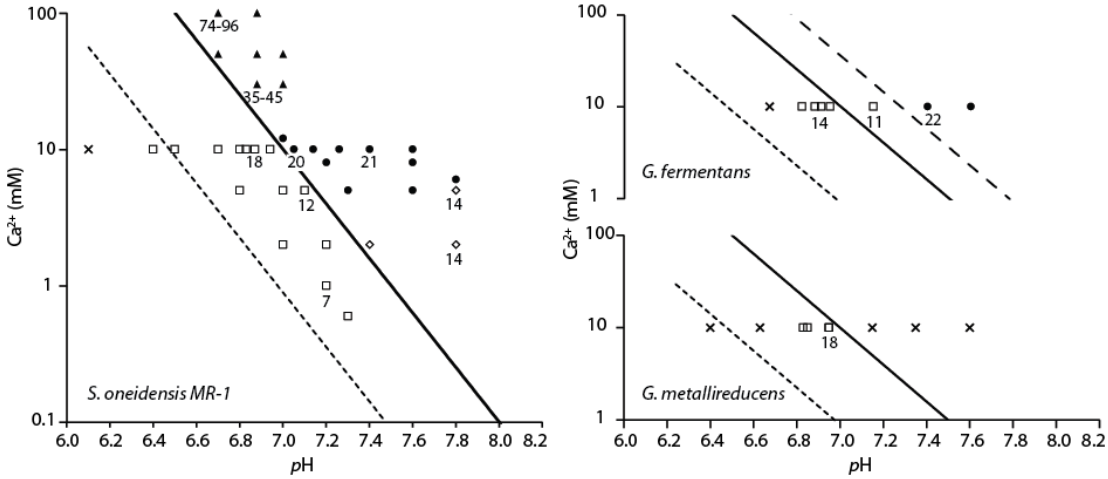

Figure 3.2. The effect of solution saturation on carbonate morphology with different iron reducing physiologies. The carbonate morphologies include rhombic (square), intermediate (diamond), spherical (circle), amorphic (triangle), and no carbonate was formed (cross). SI=1 (dotted line), SI=11 (solid line), and SI=40 (dash line). The composition of selected grains were measured, and their Ca content (mol%) are listed below the grains.

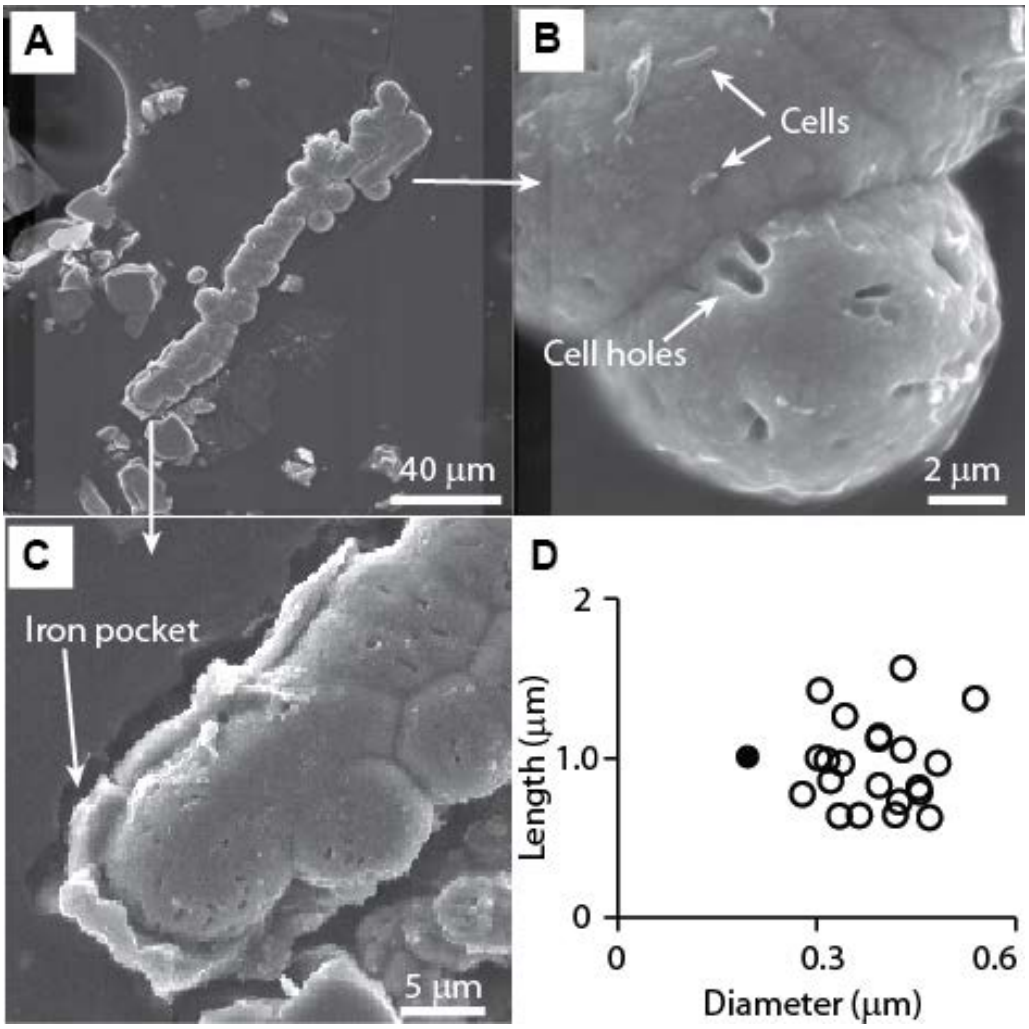

Figure 3.3. *G. fermentans* formed Long chains of fused spherical carbonate grains (A) and cell shaped micropores (B) in carbonate. (C) Ferric hydroxide pocket holds part of chain carbonate. (D) Cell shaped micropores are larger than *G. fermentans* cell.

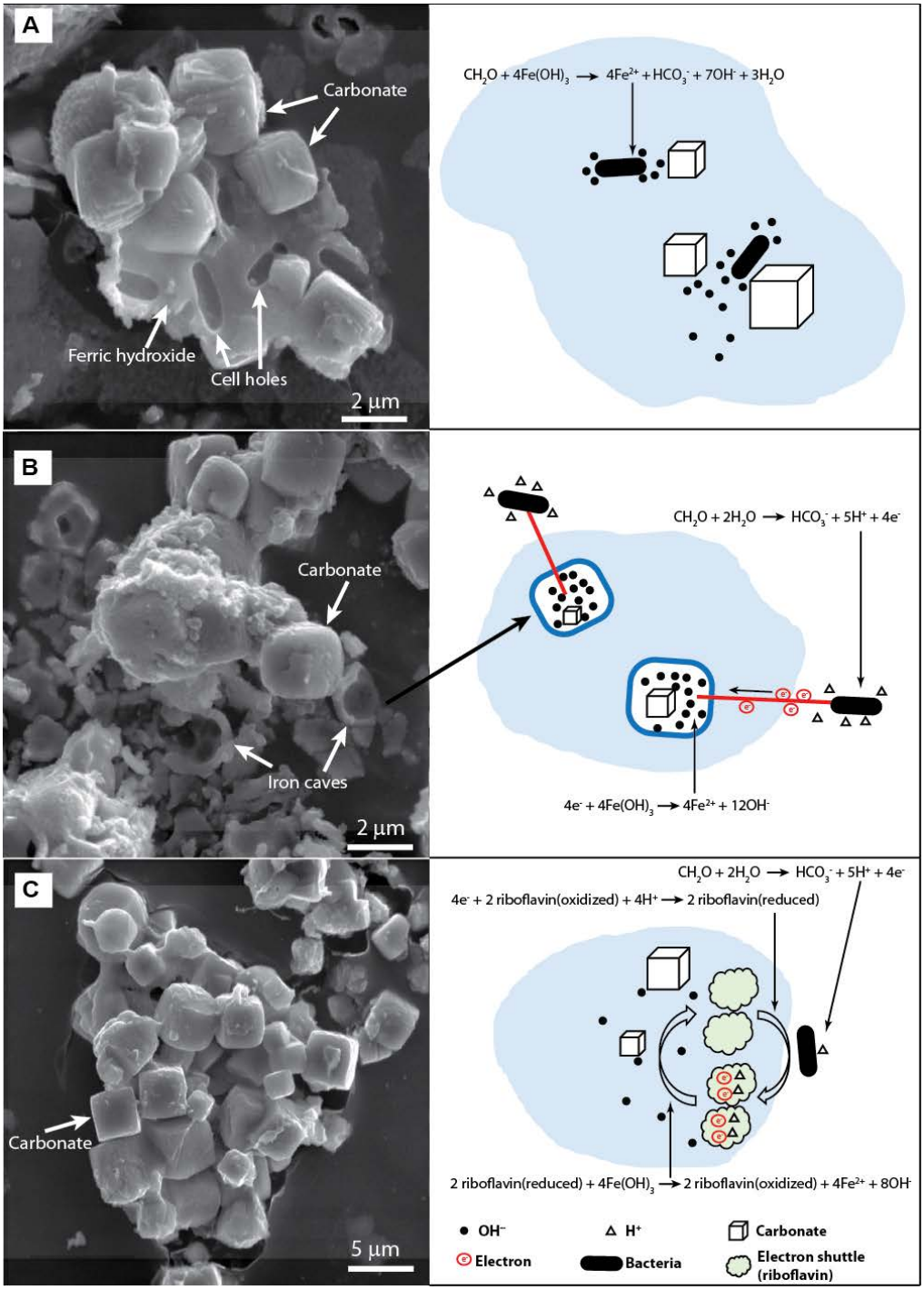

Figure 3.4. The incubation products of different physiologies, and their corresponding schematic mechanisms of physiologies shaped minerals morphology. (A) *S. oneidensis MR-1*. (B) *G. fermentans*. (C) *G. metallireducens GS-15*.

Table 3.1. Precipitates formed by different physiologies.

Physiology	Mineral composition[*]	Mineral morphology
Membrane-bound enzymes	siderite, Ca-siderite, Fe-calcite	rhombohedral[†], spherical[†]
Soluble shuttles	siderite, Ca-siderite	rhombohedra[§], spherical[*], long chaineds[#]
Nanowires	Ca-siderite	rhombohedra[§]

[*]Fig. 3.2.
[†]Fig. 3.1.
[§]Fig. 3.4.
[#]Fig. 3.3.

III.5 DISCUSSION

III.5.1 Saturation Determined Carbonate

The importance of saturation in determining carbonate morphology has been well demonstrated (Berner and Morse, 1974; Fernandez-Diaz et al., 1996). For initial calcium concentrations between 5 mM and 10 mM in *S. oneidensis MR-1* cultures, increasing initial calcite SI to 11 by increasing calcium concentration or *p*H resulted in a shift in carbonate grain morphology from rhombic to spherical, together with a correlative increase in calcium abundance in the precipitate (Fig. 3.2). Similar control of mineral morphology by supersaturation has been reported in inorganic $CaCO_3$ precipitation experiments (Fernandez-Diaz et al., 1996). At low supersaturation, crystal growth is controlled by a screw dislocation growth mechanism (Burton et al., 1951). At higher supersaturation, the growth mechanism changes to two dimensional nucleation and adhesive growth (Fernandez-Diaz et al., 1996). The grain growth mechanism is associated with grain growth rate, and growth rate is a direct function of supersaturation (Chernov, 1984). In the absence of dissolved calcium, pure siderite formed only as

rhombic grains even for *p*H as great as 8.1. This null effect of saturation on siderite morphology is consistent with inorganic siderite precipitation experiments (Romanek et al., 2009), which showed that siderite formed as rhombic grains even at extreme siderite supersaturation (SI=7000). Thus, saturation controls $CaCO_3$ grain morphology but not $FeCO_3$ grain morphology. The importance of Ca content in morphology change also is observed in the formation of intermediate carbonate grains, which were also formed under high *p*H but low Ca concentration, suggesting that incorporation of a minimal amount of Ca is necessary for forming a spherical grain even if minimal calcite saturation achieved. It is thus likely that calcite saturation controlled precipitated grain morphologies as long as enough Ca was incorporated into the grains to cause calcite-like growth mechanisms to dominate, resulting in the observed correlation between morphology and grain Ca content.

Zeng and Tice (2014) suggested that *S. oneidensis MR-1* cells increased $[Ca^{2+}]/[Fe^{2+}]$ ratios in the immediate vicinity of their cell walls by preferentially adsorbing Fe^{2+} or by precipitating iron oxides in the periplasm. This local indirect control on fluid composition caused precipitation of calcium-rich siderite during iron reduction because essentially all carbonate mineral precipitation occurred on cell surfaces. In this case, the close proximity of cell walls to the site of precipitation was critical in producing observed precipitate compositions. This interpretation is consistent with current experimental results showing that the transition between low calcium rhombic siderite and high calcium spherical siderite occurred at higher calcite

supersaturation in *G. fermentans* cultures and not at all in *G. metallireducens GS-15* cultures, neither of which were observed to nucleate carbonate precipitation.

These results suggest that the role of iron reducing bacteria in these experiments in carbonate precipitation was not to establish fundamentally different carbonate growth mechanisms, but to create locally unbalanced physicochemical microenvironments in which carbonate minerals precipitated by mechanisms similar to those observed in abiotic experiments. In turn, the morphology of precipitated carbonates reflects the power of different microbial physiologies to alter the microenvironments of precipitation.

III.5.2 Iron Reducing Physiologies Modified Carbonate

Spherical carbonate grains were precipitated when bulk solution SI was greater than 11 during *S. oneidensis MR-1* incubation, suggesting a growth mechanism dominated by to two dimensional nucleation and adhesive growth. The SI required for growth of calcite by this mechanism in inorganic experiments is 800 (Fernandez-Diaz et al., 1996), or approximately 70× greater than the threshold initial bulk solution supersaturation observed for *S. oneidensis MR-1* cultures, suggesting that these bacteria greatly enhanced local supersaturation. Enhanced supersaturation around *S. oneidensis MR-1* cells can be produced by net production of OH^-, causing HCO_3^- to deprotonate to CO_3^{2-}. Diffusion of OH^- and CO_3^{2-} away from cell surfaces would tend to drive SI toward that of the bulk solution, so enhanced supersaturation is a product of both the net stoichiometry of the oxidation/reduction reactions carried out at the cell surface and the rates of those reactions relative to diffusion.

Likewise, other electron transfer strategies and rates of reaction would determine the local distribution of Fe^{2+}, OH^- and CO_3^{2-} (Fig. 3.4). Both membrane-bound enzymes (*S. oneidensis MR-1*) and nanowires (*G. metallireducens GS-15*) would tend to concentrate OH^- in small volumes around the sites of attachment, thus achieving high local supersaturation (Fig. 3.4A and B). In contrast, because soluble electron shuttles are dispersed by random diffusion, they are unlikely to focus OH^- except in local cases where shuttle-producing organisms are densely clustered at or near the iron oxide surface (Fig. 3.4C). Moreover, when iron reduction is achieved at a distance from the cell wall, local oxidation of lactate dominates acid/base reactions, causing local consumption of OH^- and a decrease in calcite saturation around the cell. This effect likely explains the greater threshold initial calcite saturation required for precipitation of spherical grains in *G. fermentans* cultures.

G. metallireducens GS-15 cultures did not form spherical grains under any initial saturation (Fig. 3.2). Although *G. metallireducens GS-15* could theoretically concentrate OH^- more effectively on iron surfaces than *G. fermentans*, *GS-15* iron reduction rates were much lower than those of the other two cultures in all experiments (Fig. 3.5). Moreover, *G. metallireducens GS-15* also grew poorly at high *p*H, which further decreased its iron reduction rate and even halted carbonate precipitation when the *p*H was above 7.2 (Fig. 3.2). Thus, iron reduction mediated by *G. metallireducens GS-15* likely never achieved high enough local supersaturation to form spherical grains. These results suggest that some carbonate morphologies cannot be produced by certain species of iron reducing bacteria.

Long chains of fused spherical carbonate grains were produced during *G. fermentans* iron reduction (Fig. 3.3A). This distinctive form was not previously described in either inorganic or organic experiments. Organic matrix produced by bacteria has been reported to act as carbonate precipitation templates and to have affected carbonate precipitate morphologies (Defarge et al., 1996; Dupraz et al., 2009). This suggests that dissolved electron shuttle compounds (riboflavin and unknown hydrophilic quinones) produced by *G. fermentans* (Mehta-Kolte and Bond, 2012; Nevin and Lovley, 2002) could be relevant to the formation of chained carbonate. To test this hypothesis, exogenous riboflavin (1 mM) was supplied to *S. oneidensis MR-1* cultures. These additions did not produce long chained carbonate grains, but did produce short chains 3-4 grains long by adhesive growth (Fig. 3.6), suggesting that flavins may aid in chain formation but that they are not sufficient to produce observed morphologies. This suggests that chained carbonate formed by adhesive growth of dozens of spherical carbonate grains within long tunnel-like pockets carved into ferric hydroxide. These pockets likely formed as non-motile groups of cells (Coates et al., 1999) dissolved ferric hydroxide substrate, effectively boring into the iron surface. Simultaneous carbonate precipitation filled these pockets, with the electron shuttles produced by the bacteria potentially also acting to cement carbonate grains together (Fig. 3.7). Our hypothesis was also supported by the observation of a partial ferric hydroxide of carbonate chain (Fig. 3.3C).

III.5.3 Electron Transfer Strategy and Micropore Formation

Cell-shaped micropores were produced inside carbonate only by *G. fermentans* cultures. Similar micropores have been previously observed in both bacterial sulfate reduction experiments (Bosak et al., 2003) and in hot spring travertine deposits (Chafetz, 2013). The formation of these micropores was interpreted to occur in three steps (Chafetz, 2013): 1) bacteria induced carbonate precipitation around cell walls; 2) further precipitation of carbonate cement enveloped bacteria together with initial bacterially induced carbonate shells; and 3) the decay or collapse of dead cells formed micropores within carbonate. This model is unlikely to explain carbonate micropores observed in the current study.

The ability of cells to move may have influenced micropore formation in precipitated carbonate grains. The only carbonate micropores observed in this study were formed by the non-motile *G. fermentans*, likely because they were trapped by growing carbonate, thus leaving cell-shaped cavities. Notably, micropore sizes were about twice as large as *G. fermentans* cells. This was probably because oxidation of lactate decreased *p*H in the micro-space outside the cell surface, and thus inhibited carbonate precipitation in this volume (Fig. 3.6F). It is also possible that EPS coated on cell surfaces inhibited carbonate precipitation by binding metal ions (e.g. Ca^{2+} and Fe^{2+}), and thus decreasing free metal ion activity for carbonate precipitation (Dupraz et al., 2009). However, this effect was not observed in other cultures. In either case, living bacteria cells were protected from carbonate lithification on cell membrane directly, but continued carbonate growth eventually encased the entire non-mobile bacterial cell

inside carbonate. Therefore, lack of motility results in the capture of bacterial cells by carbonate, and the acidic cell wall and/or presence of EPS inhibited carbonate growth around cells and thus produced micropores larger than the cells in carbonate.

The formation of different shapes of micropores in iron mineral, such as the cell-shaped micropores by *S. oneidensis MR-1*, caves by *G. metallireducens GS-15*, and tunnel-like pockets by *G. fermentans*, preserve even more information about biological processes than do micropores in carbonate, because they reflect the strategies applied by bacteria to contact and dissolve solid minerals (Fig. 3.5). Despite this, reported observations of micropores in iron oxide minerals are extremely rare, either because they are difficult to preserve or because their significance has not been recognized. Microbial iron reduction commonly occurs with reduction of other metals *via* the same biological mechanisms (DiChristina et al., 2002), suggesting that similar micropores could also form in other reducible metal minerals (e.g., those containing Fe(III), Mn(IV), Cr(IV), Ce(IV) or even S(VI)). Therefore, micropores formed in reducible minerals could serve as biosignatures for the evolution of microbial mineral reduction.

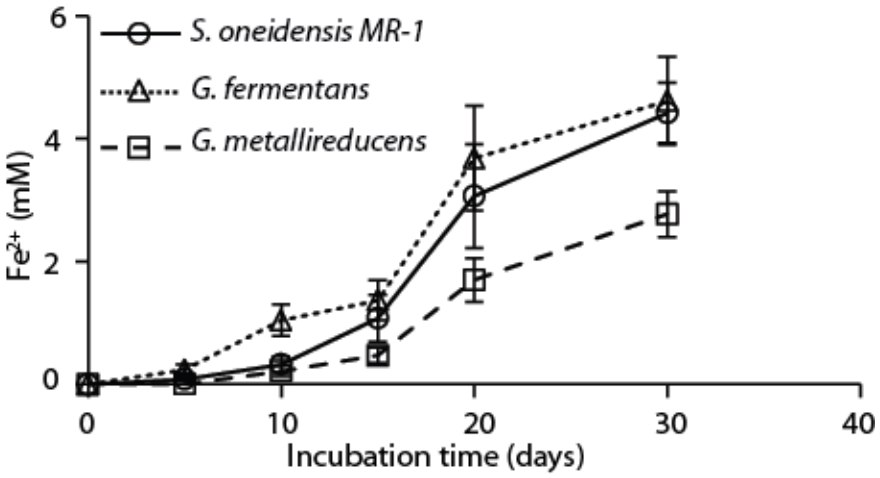

Figure 3.5. The iron reduction rate of three strains. *G. metallireducens GS-15* was significant slower than *S. oneidensis MR-1* and *G. fermentans* at neutral *p*H (6.7).

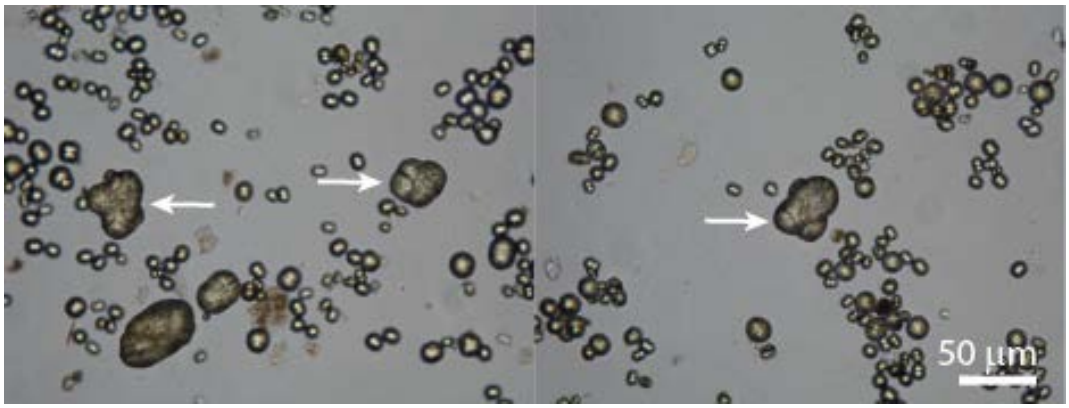

Figure 3.6. Added exogenous riboflavin to *S. oneidensis MR-1* culture induced adhesive carbonate growth (arrows).

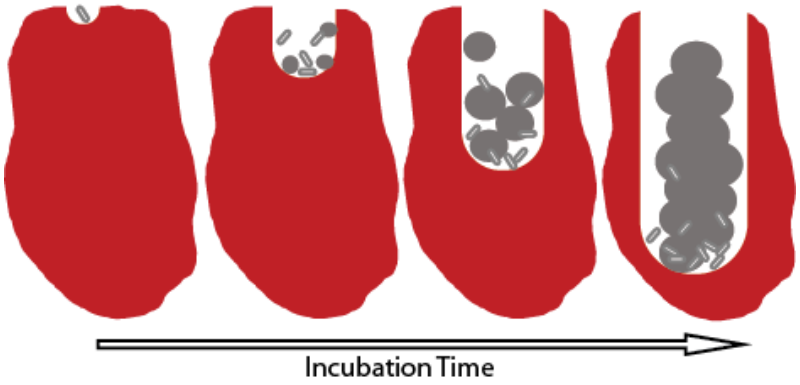

Figure 3.7. Schematic formation of long chains of fused spherical carbonate grains by *G. fermentans*. Red represents iron mineral, gray represents siderite, and clear rods represent bacterial cells.

III.6 CONCLUSIONS

Iron reducing physiologies, including membrane bound enzymes, electron shuttles and nanowires, apply different strategies to transfer electrons to solid iron minerals and thus regulate the morphology of precipitated carbonate and micropore formation. Iron reduction rate and location of iron reduction relative to the cell surface together determine the level of local saturation to precipitate corresponding carbonate morphologies (rhombohedral or spherical). Long chained carbonate was only formed by *G. fermentans*, and its non-motile character and extracellular electron shuttle (riboflavin) is responsible for this special morphology. Micropores induced by different iron reducing physiologies, for instance, cell shaped and cave like micropores in iron oxide were formed by *S. oneidensis MR-1* and *G. metallireducens GS-15* respectively, and expansive cell shaped micropore in carbonate was formed by *G. fermentans*, can be a

potent biosignature, because the type of micropore is not just recording microbial iron reduction but also correlates with a certain iron reducing physiology.

CHAPTER IV

BIOTIC AND ABIOTIC MECHANISMS OF CERIUM REDOX CYCLING

IV.1 OVERVIEW

The cerium anomaly is an important and commonly applied paleoproxy for the presence of molecular oxygen in ancient fluids (Elderfield, 1988; Moffett, 1990; Wright et al., 1987). However, the mechanisms of cerium oxidation and reduction in nature are not well understood. Although Ce(III) is likely oxidized along with manganese by a common biological pathway (Moffett, 1990), no specific organisms or mechanisms have been identified connecting oxygen and cerium oxidation. Likewise, Ce(IV) is reduced in suboxic zones (German and Elderfield, 1989), but reduction mechanisms have not been identified. We tested for Ce(III) oxidation activity on agar plates and in liquid medium with *Roseobacter sp*. AzwK-3b, a known manganese oxidizing bacterium, and measured cerium reduction by incubation of Ce(IV) with *Shewanella oneidensis MR-1* (a metal reducing bacterium), as well as Fe^{2+} and Mn^{2+} individually. We found that Ce(III) oxidation was mediated by *Roseobacter sp*. AzwK-3b through the production of extracellular superoxide. Ce(IV) was directly reduced by *Shewanella oneidensis MR-1*, as well as by Fe^{2+} and Mn^{2+} abiotically. We therefore conclude that bacteria can directly or indirectly mediate cerium redox cycling.

IV.2 INTRODUCTION

Cerium is the only rare earth element with an active redox chemistry at Earth surface temperatures, making comparison between it and the similarly-sized rare earths La, Pr, and Nd (the "cerium anomaly") an important paleoredox proxy (Elderfield, 1988; Moffett, 1990). Moffett demonstrated that Ce(III) oxidation is catalyzed by marine microorganisms (Moffett, 1990) by showing that oxidation in marine fluids is inhibited by the metabolic inhibitor sodium azide (Moffett, 1990). He further suggested that Ce oxidation shares a closed mechanistic pathway with manganese oxidation in marine environments (Moffett, 1994). However, specific biological pathways of Ce(III) oxidation are not currently known.

Roseobacter sp. AzwK-3b is known to indirectly oxidize Mn by producing extracellular superoxide rather than by a specific enzymatic pathway (Hansel et al., 2011). The broad distribution of the *Roseobacter* clade in oceans worldwide suggests that they might contribute to metal cycling by releasing superoxide to the water column (Gonzalez and Moran, 1997; Hansel et al., 2011). Superoxide is known to oxidize cerium (Heckert et al., 2008) (equation 4.1).

$$O_2^{\cdot -} + Ce^{3+} + 2H_2O \rightarrow H_2O_2 + CeO_2 + 2H^+ \quad (4.1)$$

Therefore, we hypothesized that *Roseobacter sp*. AzwK-3b could mediate Ce(III) oxidation by superoxide production, thus providing a biological link between Ce and Mn oxidation in seawater.

Ce(IV) reduction takes place in suboxic environments (German and Elderfield, 1989); however, specific mechanisms of reduction under these conditions are not known.

Dissimilatory metal reducing bacteria (e.g. *Shewanella spp.*) play a critical role in metal cycling by reducing and releasing metal ions from sediments into pore fluids (Lovley, 1991). It is possible that bacteria can also reduce cerium directly or through the byproducts of other metal reduction pathways. Identifying the role of bacteria in cerium reduction will lead to a better understanding of processes modifying or overprinting primary cerium anomalies in sediments.

IV.3 MATERIALS AND METHODS

IV.3.1 Determination of Microbial Cerium Oxidation

Roseobacter sp. AzwK-3b was cultivated at 30°C and 150 rpm in modified K medium prepared with 75% artificial seawater at pH 7.2 (Templeton et al., 2005). To eliminate the effect of transition metal ions (especially Fe^{2+} and Mn^{2+}) on cerium oxidation, all trace elements were removed from original K medium.

Cerium oxidation assay plates were made with modified K medium, 1.5% agar, and with or without 100 µM of $CeCl_3$. Cerium oxidation was monitored by formation of pink (pink-colored formazan) colonies and halos on plates after staining with IHTC dye (Hashmi and Rashid, 1966). IHTC was prepared by mixing equal volumes of 0.2% isonicotinic acid hydrazide solution and 0.2% of 2, 3, 5-triphenyltetrazolium chloride solution. To process the assay, 1 ml of 0.25N H_2SO_4 was added to the plate with mature colonies. 4 ml of nanopure water were then added, followed by addition of 2 ml of freshly prepared IHTC. The appearance of pink colonies in 5 min after adding IHTC indicates the presence of Ce(IV).

To determine cerium oxidation in liquid samples, *Roseobacter sp*. AzwK-3b was inoculated in modified K medium at 30°C, 150 rpm. Cell-free filtrate was prepared following Learman's protocol (Learman et al., 2011). $CeCl_3$ or $MnCl_2$, and with or without SOD (5µM) were added to 10 ml of filtrate aliquot at a final concentration of 100 µM and incubated at room temperature for 90 hours. All treatments were run in triplicate. Incubated filtrate samples were centrifuged at 5000 × g for 20 min. The supernatant was then removed and the pellets re-suspended with 1 ml of 0.25 N H_2SO_4, diluted with 4 ml of nanopure water and 2 ml of freshly prepared IHTC. Each sample was allowed to stand for 5 min. After mixing with 1 ml of n-amyl alcohol, each sample was centrifuged, and the separated organic layer was measured by spectrophotometry at 490 nm. $Ce(SO_4)_2$ was used as a standard.

$MnCl_2$ was used as a positive control to estimate the production of superoxide by *Roseobacter sp*. AzwK-3b in cell free filtrate experiments. Mn oxidation was measured with Leucoberbelin blue (LBB) assay (Devrind et al., 1986).

IV.3.2 Determination of Microbial Cerium Reduction

To reduce cerium, *Shewanella oneidensis MR-1* was incubated in basal medium contained 10 mM NH_4Cl, 0.1 mM $MgCl_2$, 0.1 mM KH_2PO_4, 0.5 g/L of casamino acid, 20 mM 4-(2-hydroxylethyl)-1-piperazineethanesulfonic acid (HEPES), 1 mM $Ce(SO_4)_2$ (electron acceptor), and 20 mM lactate (electron donor). Basal medium was titrated in anaerobic chamber (88% N_2, 7% CO_2 and 5% H_2) and adjust *p*H to 7.0 before inoculated with *S. oneidensis MR-1*. Both biotic samples and abiotic controls were run in triplicate at room temperature (23°C).

To analyze samples, 2 ml of homogenous samples were extracted from sealed bottles with needles during 0, 2, 5, 12, 20 and 30 day incubation periods. Small aliquot of extracted samples were diluted to proper concentrations for plate counting to estimate the number of viable bacterial cells. Based on Ce(IV) has absorbance in the 300-400 nm range (Medalia and Byrne, 1951), absorbance at 350 nm was collected to quantify Ce(IV) (Beckman DU Series 700). IHTC assay was also used to analyze the 0 and 30-day incubation samples to determine the amount of Ce(IV).

The 30-day incubation samples were washed with nanopure water and dried for X-ray diffraction (XRD) (Bruker D8) analysis with Cu-*K*α radiation at an accelerating voltage of 35 kV and a filament current of 45 mA.

IV.3.3 Determination of Abiotic Cerium Reduction

Abiotic cerium reduction experiment was conducted in 96-well plates at room temperature (23 ˚C). Each well contained 0.25 mM of $Ce(SO_4)_2$, and 0.25 mM of $FeSO_4$ or $MnCl_2$ at a total volume of 200 µl. The controls only contained 0.25 mM of each above compound. All treatments and controls were performed 9 replicates, and the incubation of $Ce(SO_4)_2$ and $MnCl_2$ were conducted in the anaerobic chamber. IHTC assay was used to measure the concentration of Ce(IV) per well: 50 µl of 0.25N H_2SO_4 was added to each well, then 100 µl of IHTC dye were added and incubated for 5 min. The absorbance at 490 nm was measured with a microplate reader (BioTek, ELx800). $Ce(SO_4)_2$ and $FeSO_4$ mixing sets were duplicated for Fe(II) measurement with the ferrozine assay(Viollier et al., 2000). Oxidized Mn was measured with the LBB assay (Devrind et al., 1986).

IV.4 RESULTS

IV.4.1 Cerium Oxidation

Roseobacter sp. AzwK-3b was tested for Ce(III) oxidation activity during growth on K medium agar plates amended with 100 µM $CeCl_3$. When grown on Mn(II)-amended plates, *Roseobacter sp*. AzwK-3b forms brown haloes due to the presence of Mn(III,IV) oxides; however, CeO_2 is light yellow to white and there is very little visual difference between plates inoculated with or without $CeCl_3$. Isonicotinic acid hydrazide and 2,3,5-triphenyltetrazolium chloride (IHTC) dye (Medalia and Byrne, 1951) were therefore used to stain plates after growth, causing pink haloes and colonies to appear on plates with amended with Ce (Fig 4.1A). Ce-free and abiotic control plates and areas outside of colonies haloes did not turn pink (Fig. 4.1B). Because IHTC turns pink following oxidation by Ce(IV), this result indicates that Ce(III) was oxidized to Ce(IV) by *Roseobacter sp*. AzwK-3b.

Cell free filtrate was made to test the hypothesis that superoxide produced by *Roseobacter sp*. AzwK-3b was responsible for observed cerium oxidation. Cultures reached stationary phase after 50-60 hours of incubation, at which time superoxide production was maximal as indicated by Mn(II) oxidation activity (Fig. 4.2A). Aliquots of filtrate with cerium showed good correlation between cerium oxidation and superoxide production (Mn oxidation) (Fig. 4.2B). Moreover, filtrate did not oxidize cerium in the presence of superoxide dismutase (SOD) (Fig. 4.2B), indicating cerium was oxidized by extracellular superoxide rather than through an enzymatic pathway. However, superoxide can also reduce Ce(IV) to Ce(III):

$$O_2^{\cdot -} + Ce^{4+} \rightarrow Ce^{3+} + O_2 \quad (4.2)$$

Thus, the net production of Ce(IV) is determined by the relative rates of the oxidation and reduction steps, and net measured oxidation in these experiments was low (5%; Fig. 4.2). In nature, Ce(IV) would be protected from re-reduction by precipitation and adsorption to sinking particles, likely producing more complete oxidation than observed here.

IV.4.2 Microbial Cerium Reduction

When $Ce(SO_4)_2$ was provided as the only electron acceptor in *S. oneidensis MR-1* incubation, a decrease of Ce(IV) density was observed (Fig. 4.3). Loss of Ce(IV) was coupled to *S. oneidensis MR-1* growth (Fig. 4.3), suggesting that Ce(IV) may be reduced by *S. oneidensis MR-1*. In addition, a Ce(III) mineral identified as $Ce_2(SO_4)_3 \cdot nH_2O$ by X-ray diffraction was precipitated during Ce(IV) reduction (Fig. 4.4). Note that precipitation of this mineral in natural sediments is unlikely because of the very low concentration of cerium marine fluids (~10 pM) (Sholkovitz and Schneider, 1991), or approximately 8 orders of magnitude less than in our experimental incubations.

IV.4.3 Abiotic Cerium Reduction

The standard electrode potential ($E°$) of Fe^{3+}/Fe^{2+}, Mn^{4+}/Mn^{2+} and Ce^{4+}/Ce^{3+} are 0.95, 1.29 and 1.58 V, respectively (Heckert et al., 2008). The reductant with lower $E°$ can reduce an oxidant with a larger $E°$. Therefore, Fe^{2+} and Mn^{2+} are able to reduce Ce^{4+} thermodynamically (equation 4.3). Our results showed that Fe^{2+} quickly reduced $Ce(SO_4)_2$ in seconds, with the amount of $Ce(SO_4)_2$ reduction equaling the amount of Fe^{2+} oxidation (P =0.33 for a t-test on the means) (Fig. 4.5). When $Ce(SO_4)_2$ and Mn^{2+} were

combined anaerobically, white cerium particles turned dark brown and the formation of Mn(III) or (IV) was detected by LBB assay (Fig. 4.6). Although the reduction of Ce(IV) cannot be directly detected by the IHTC assay because IHTC can also be oxidized by Mn(II,IV) oxide, Mn oxidation required the presence of $Ce(SO_4)_2$, suggesting that Ce(IV) was reduced by Mn^{2+}.

$$Fe^{2+}/Mn^{2+} + Ce^{4+} \rightarrow Fe^{3+}/Mn^{3+} + Ce^{3+} \quad (4.3)$$

IV.5 DISCUSSION

Ce oxidation is mediated by the superoxide generated by bacteria, suggesting that Ce oxidation could be associated with the distribution of superoxide producers. Field studies show that the vertical distribution and concentration of superoxide in seawater is highly variable and changes with location in the ocean (Rose et al., 2008; Rusak et al., 2011), yet it is generally believed that superoxide is most abundant in the photic zone due to the activity of phytoplankton (Rusak et al., 2011). Indeed, intense cerium oxidation has been observed in the surface 200 m of the water column (Alibo and Nozaki, 1999). However, in some cases heterotrophic bacteria such as *Roseobacter sp*. AzwK-3b produce superoxide more rapidly than cyanobacteria (Learman et al., 2011), which may result in more intense production of superoxide in deep and dark water than in the photic zone (Rose et al., 2008; Vermilyea et al., 2010). This potentially explains Moffett's observation that the lower photic zone had greater cerium oxidation rates than upper photic water and that cerium oxidation was most rapid in the dark (Moffett, 1990). Nevertheless, there is strong evidence to support the association of superoxide

production and cerium oxidation in seawater, but a simultaneous measurement of superoxide concentration and cerium oxidation rate in seawater is still essential for further study.

Cerium reduction takes place under suboxic conditions in sediments (German and Elderfield, 1989). In our study, cerium was quickly reduced abiotically by both Fe^{2+} and Mn^{2+}, suggesting that fast reduction and remobilization of cerium could occur in metal reducing sediments. Cerium undergoing reduction in the presence of Fe^{2+} and Mn^{2+} links the cerium reduction to microbial iron and manganese reduction. In addition, Ce(IV) can reduced directly by a common metal-reducing bacterium, indicating that both biotic and abiotic pathways may be active in the reductive loop of the cerium cycle.

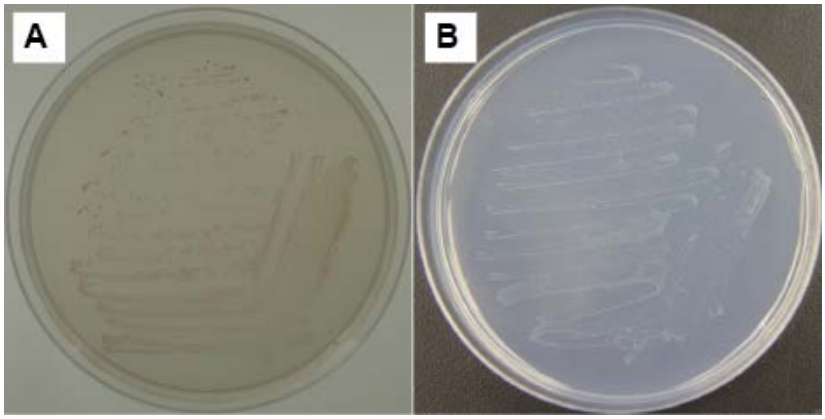

Figure 4.1. (A) In the presence of 100 µM $CeCl_3$, *Roseobacter sp*. AzwK-3b colonies exhibited pink color with IHTC dye, indicating Ce(III) was oxidized to Ce(IV). (B) Control, absent of $CeCl_3$.

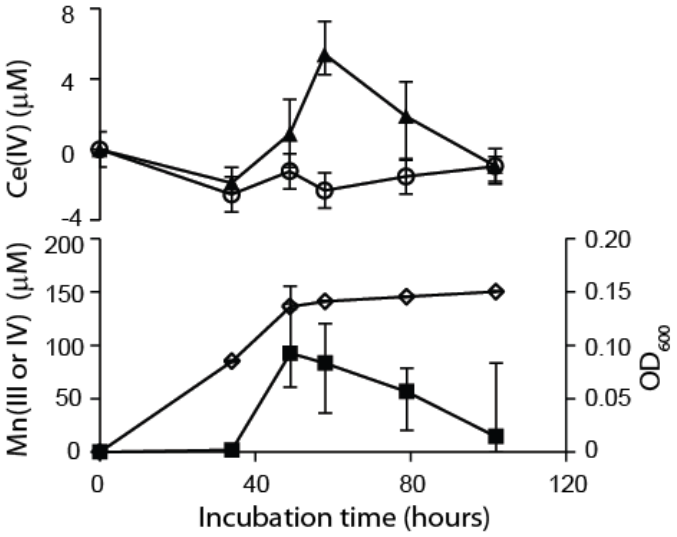

Figure 4.2. *Roseobacter sp*. AzwK-3b mediated Ce(III) oxidation by generating superoxide. Ce(III) was oxidized to Ce(IV) (solid triangles), and SOD inhibited Ce oxidation (open circles). Open diamonds indicate culture density of *Roseobacter sp*. AzwK-3b. Mn oxidation was used as control to evaluate superoxide production during bacterial growth (solid squares).

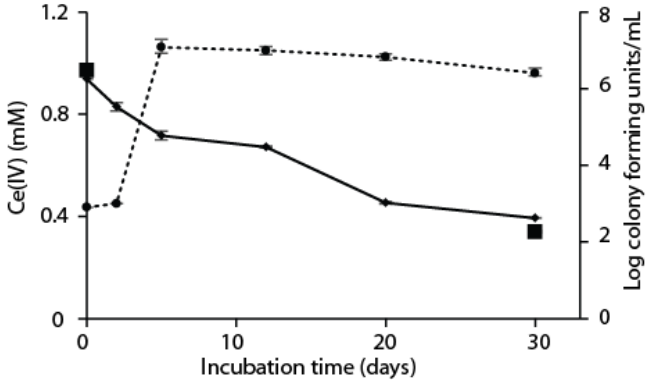

Figure 4.3. Both spectrophotometric (solid line) and IHTC assay (square) indicated loss of Ce(IV) during *S. oneidensis MR-1* incubation. The growth of *S. oneidensis MR-1* (dotted line) was coupled with cerium reduction.

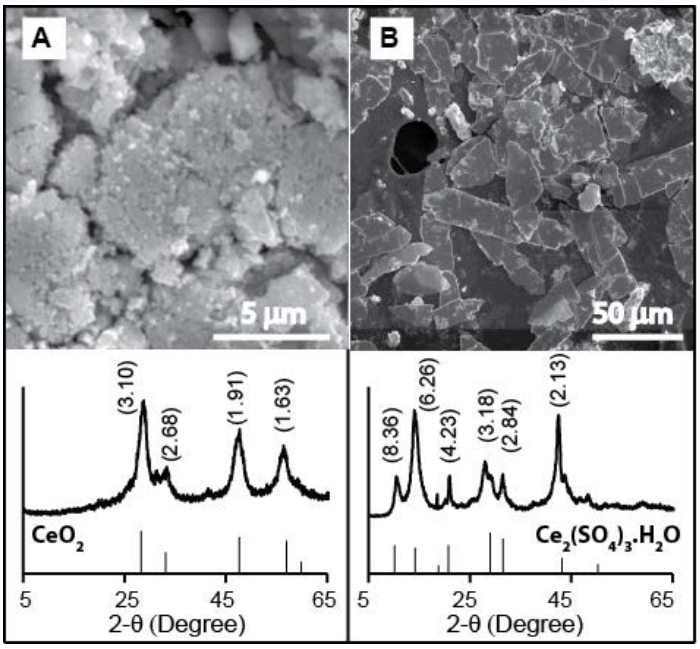

Figure 4.4. XRD analysis of minerals produced during *S. oneidensis MR-1* Ce(IV) reduction. (A) Abiotic control; mineral is CeO_2. (B) *S. oneidensis MR-1* reduced Ce(IV) and formed $Ce_2(SO_4)_3 \cdot H_2O$.

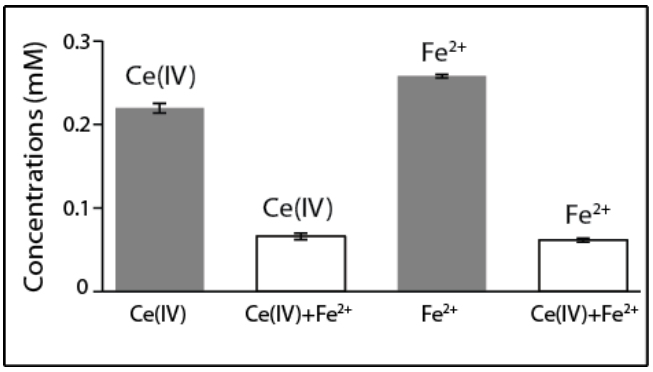

Figure 4.5. Ce(IV) was reduced in the presence of Fe^{2+}, and a nearly equal amount of Fe^{2+} was oxidized at the same time. The redox reaction of Ce(IV) with Fe^{2+} is described in equation 4.3.

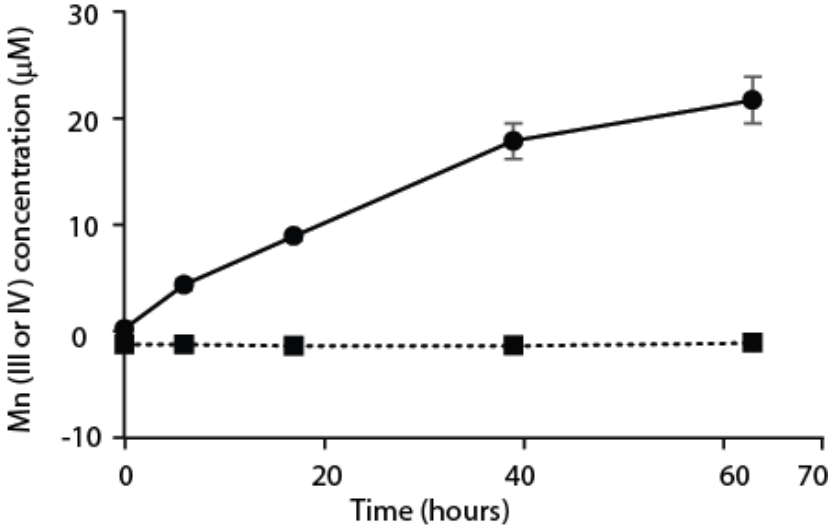

Figure 4.6. Mn^{2+} was oxidized to Mn(III,IV) in the presence of $Ce(SO_4)_2$ anaerobically, suggesting that Ce(IV) was reduced by Mn^{2+} as well. Circles indicate Mn^{2+} in solution with $Ce(SO_4)_2$; squares indicate control (only Mn^{2+}).

CHAPTER V

IRON FERTILIZATION OF PRIMARY PRODUCTIVITY BY VOLCANIC ASH IN THE LATE CRETACEOUS (CENOMANIAN) WESTERN INTERIOR SEAWAY

V.1 OVERVIEW

Volcanic ash contains 1-10% FeO by weight and can be a significant contributor of Fe to the surface ocean (Duggen et al., 2010). It is possible that Fe fertilization by volcanic ash has contributed to marine productivity in the past. The Late Cretaceous Eagle Ford Group (Cenomanian/Turonian) contains abundant volcanic ash beds interbedded with black argillaceous limestones and marls, providing opportunities for observation of the influence of ash on productivity and basin chemistry in the Western Interior Seaway. A 49-m-thick core sample containing 51 visualized ash beds with varying thickness was collected through the Lower Eagle Ford and the basal Upper Eagle Ford from south Texas was scanned by x-ray *fluorescence* spectroscopy to examine burial of Fe, trace elements delivered to the sediment by sinking organic matter (Ni), and paleoredox proxies (Mo and Cr) below, in, and above ash beds.

Ash beds and beds containing admixed ash contain much more Fe than interbedded black shales, suggesting that ash transported reactive Fe to otherwise Fe-poor settings. The contents of Mo and Ni were significantly greater in beds with admixed ash than in surrounding beds. In contrast, Cr was less abundant in the beds with greatest ash content. These observations imply that input of ash increased marine productivity (elevated Ni), which in turn enhanced oxygen demand and promoted

euxinia (elevated Mo and lower Cr). We conclude that Fe-bearing volcanic ash fertilized the southern Cenomanian Western Interior Seaway.

V.2 INTRODUCTION

Iron is a critical nutrient for phytoplankton growth (Coale et al., 1996), and iron limitation has been observed in several areas of the modern ocean (Behrenfeld et al., 1996; Hutchins and Bruland, 1998) and inferred for the Southern Ocean during the last glacial maximum (Watson et al., 2000). Volcanic ash contains 1-10% FeO by weight and can be a significant source of iron to the surface ocean (Duggen et al., 2010). Because it is rapidly released from ash to the water column, iron becomes bioavailable to phytoplankton in the surface ocean, and thus can enhance primary productivity (Frogner et al., 2001). Consequently, iron fertilization by ash has the potential to have a significant impact on carbon sequestration and long term climate (Blain et al., 2007).

However, the effect of volcanic ash deposition on ocean fertilization is uncertain in the past because little is known about how prevalent iron limitation has been in oceans throughout Earth history (Duggen et al., 2010). The Late Cretaceous Eagle Ford Group (Cenomanian/Turonian) contains abundant volcanic ash beds interbedded with black argillaceous limestones and marls. In south Texas, these rocks were deposited in relatively quiet-water environments with minimal reworking by currents or organisms, providing opportunities for observation of the influence of ash on productivity and basin chemistry in the southern Western Interior Seaway.

Trace metal abundances were applied as paleoproxies for water column reduction state and productivity (Algeo and Maynard, 2004; Tribovillard et al., 2006). For instance, Mo is preferentially accumulated in sediments deposited under euxinic water columns (containing free sulfide), Cr tends to be enriched under anoxic but not euxinic conditions, and Ni accumulation indicates high organic productivity even if organic matter was totally or partially decomposed (Tribovillard et al., 2006).

V.3 MATERIALS AND METHODS

The study site is located in McMullen County, Texas, which was at the southern edge of the Western Interior Seaway during the Cenomanian and approximately 100 kilometers from land (Fig. 5.1). 49 meters of 10 cm diameter core was collected through the Eagle Ford Group and cut in half vertically for scanning by X-ray *fluorescence* spectrometer (XRF) every 5 mm. Volcanic ash beds were recognized under ultraviolet light based on their orange fluorescence, whereas admixed ash was recognized by its elevated Al and Ti fluorescence. Selected samples were scanned by high resolution (100 μm) X-ray analytical microscopy (μXRF, XGT-7000, Horiba Jobin-Yvonne).

V.4 RESULTS AND DISCUSSION

The sampled core consists of the upper Buda Formation (Early Cenomanian) and part of the Eagle Ford Group deposited during the Late Cenomanian (including the Lower Eagle Ford and the basal Upper Eagle Ford). The contact between dark organic-rich marls of the Eagle Ford Group with the underlying gray limestone of the Buda

Formation is sharp and clearly recognizable in XRF data (e.g. Al, Mo, and Cr; Fig. 5.2). The boundary between the Lower and Upper Eagle Ford is poorly defined lithologically from core. However, this contact is marked in other locations by an abrupt decrease in Mo abundance. Such a decrease is identifiable in this core, and we provisionally identify the Upper Eagle Ford boundary at this location (Fig. 5.2).

51 ash beds with thicknesses ranging from 0.1-5.5 cm were identified visually in the Eagle Ford section of the core, but none were observed in the Buda section. Al, Ti and Fe fluorescences were each highly correlated with each other and with ash beds (Figs. 5.2 and 5.3), with abundances typically decreasing upward from these layers. This observation suggests that these elements were derived from ash, with high and intermediate abundances reflecting relatively pure ash beds or trace ash content in ambient marls, respectively, and allows identification of ash in the Buda section (Fig. 5.2). Ash beds and beds containing admixed ash contain much more Fe than interbedded black marls (Fig. 5.3), suggesting that ash transported Fe to otherwise Fe-poor settings.

Mo is a useful paleoproxy for euxinic conditions because it binds to pyrite and organic matter in the presence of sulfide (Algeo and Maynard, 2004). Mo content is much higher in the Lower Eagle Ford than in the Buda and the Upper Eagle Ford (Fig. 5.2), even controlling for variable ash content (Fig. 5.4). Variable response of Mo to ash content by stratigraphic unit suggests that Mo was not deposited primarily as a primary component of the ash and that authigenic Mo accumulation was responsible for the Mo enrichment in the Lower Eagle Ford. Thus, Mo enrichment implies that the water

column was episodically strongly euxinic during deposition of the Lower Eagle Ford Group.

Mo fluorescence is greatest in Lower Eagle Ford ash beds (Fig 5.3). The close correlation between Mo and ash beds in this unit is likely due to the presence of pyrite in these beds (Fig. 5.3), as Mo is preferentially captured by authigenic pyrite (Algeo and Maynard, 2004). However, abundant pyrite in the Upper Eagle Ford contains very little Mo, indicating that Mo was not universally associated with pyrite. Instead, Mo is incorporated into pyrite only under euxinic conditions (Algeo and Maynard, 2004). This observation indicates that late diagenetic fluids are unlikely to have produced Mo enrichments or associations with ash, because pyrite in all three units should otherwise contain similar Mo abundances. Therefore, the enrichment of Mo in ash beds suggests that ash deposition enhanced euxinic conditions during Lower Eagle Ford deposition.

Cr is reduced and precipitated primarily along with Fe and Mn in anoxic environments, and thus acts as a proxy for anoxic but not euxinic conditions (Algeo and Maynard, 2004). Cr fluorescences in the Lower Eagle Ford section are intermediate to those in the Upper Eagle Ford and Buda sections (Fig. 5.2), in contrast to Mo fluorescences, which are greatest in the Lower Eagle Ford. These data support the interpretation of the Lower Eagle Ford as the deposits of a euxinic ocean and suggest that the Upper Eagle Ford was deposited in an episodically anoxic but not euxinic environment (Fig. 5.2). Cr and Mo fluorescence are inversely correlated in most thick Lower Eagle Ford ash beds (Fig. 5.3). A similar relationship to ash is observed throughout the Lower Eagle Ford, with Cr positively correlated with Al at low Al

fluorescence and negatively correlated with Al at high Al fluorescence (Fig. 5.4). Because Cr can neither be precipitated in euxinic conditions nor incorporated into pyrite (Algeo and Maynard, 2004), this relationship confirms that strongly euxinic conditions prevailed as ash beds were deposited. Thus, Cr fluorescence relationships indicate that the Upper Eagle Ford was deposited under range of redox conditions from oxic to anoxic, and supports the conclusion that ash input enhanced reducing conditions throughout deposition of much of the Eagle Ford Group.

Ash beds in all units contain variable but elevated Ni abundances relative to surrounding marls. Highly variable Ni enrichment in ash beds (Fig. 5.3) suggests that Ni was not a major primary component of ashes prior to deposition. Ni is transported to sediments primarily by adsorption to sinking organic matter and retained in reducing sediments by incorporation in authigenic pyrite during later organic matter decay (Algeo and Maynard, 2004), making it an effective paleoproxy for primary productivity. In this case, ashes associated with high productivity (high Ni/Al fluorescence ratio) should also be associated with more reducing conditions (high Mo/Al fluorescence ratio), and with more authigenic pyrite (high Fe/Al fluorescence ratio) as well. This is observed throughout the Lower Eagle Ford section (Fig. 5.5), supporting the conclusion that ash deposition was associated with elevated productivity in the overlying water column.

Iron fertilization can promote a 3-4 times increase in productivity in iron-limited areas of the modern ocean (Martin et al., 1994). Although the residence time of volcanic ash in the euphotic zone is only a few minutes to a few days depending on particle size (Duggen et al., 2007), rapid iron release from these particles (37 $\mu M\ g^{-1}\ h^{-1}$) (Frogner et

al., 2001) may generate sufficient iron to influence ocean ecosystems. Duggen et al. (2007) suggested that deposition of 1 mm of ash layer can increase the concentration of iron by a few nM in seawater, which is sufficient to stimulate phytoplankton blooms (Wells, 2003). Phytoplankton respond to iron input within 24 hours and deplete major nutrients from surface water within 5-7 days (Martin et al., 1994), implying that ash deposition and productivity enhancement occur almost simultaneously. In contrast, elevated atmospheric CO_2 concentrations and temperatures following extensive volcanic activity would tend to increase productivity less and over longer time scales (Lee et al., 2013). Thus, the strong covariance between Ni (productivity) and Mo (euxinia), and ash beds in the Lower Eagle Ford indicates that inferred productivity enhancements were effected by rapid iron fertilization rather than by increased CO_2 and temperature. Understanding the relationship between volcanism and productivity in the past is important because carbon burial following volcanic activity may have played a critical role in regulating Cretaceous climate (Lee et al., 2013). We suggest that Cretaceous volcanism persistently loaded substantial amounts of iron-bearing ash into the Western Interior Seaway, increasing productivity and oxygen demand in sediments, and thus promoting anoxia and euxinia during Eagle Ford time. Volcanic ash fertilization thus likely played a significant role in carbon sequestration in parts of the Late Cretaceous ocean.

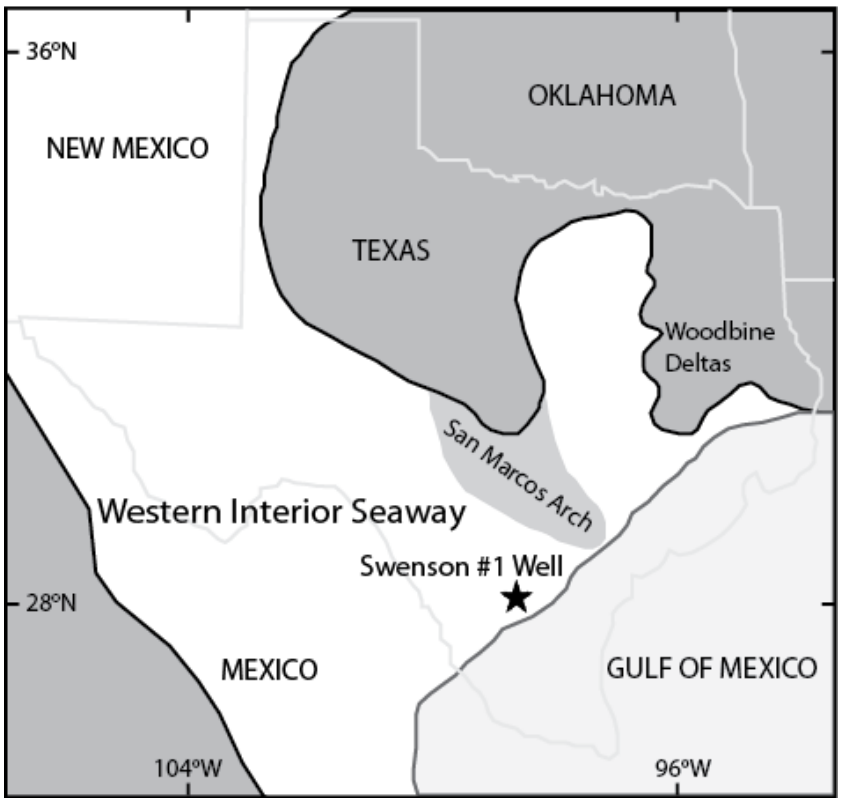

Figure 5.1. Paleographic map of Texas during late Cretaceous with the location of Swenson #1 core. Map was modified from (Denne et al., 2014).

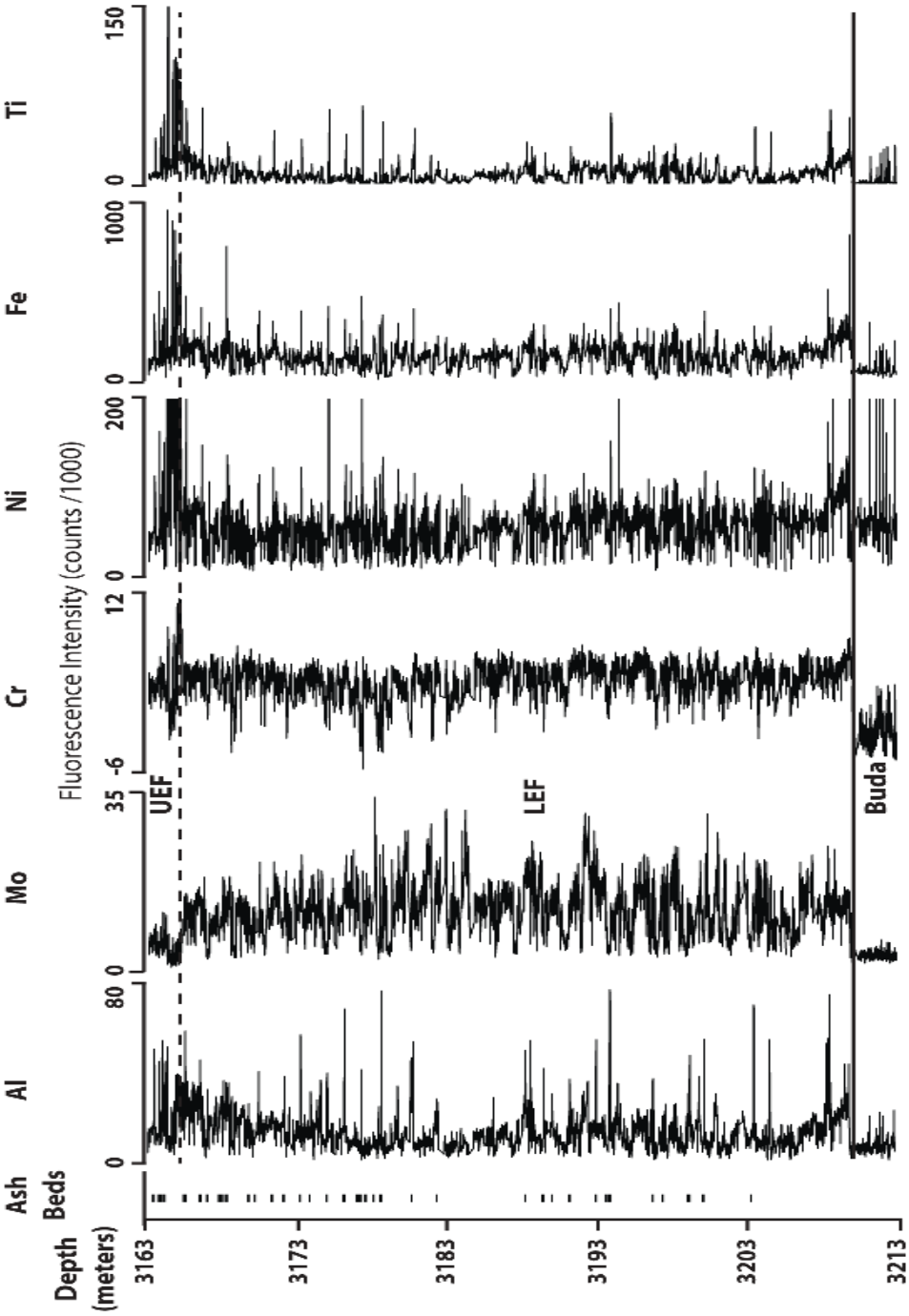

Figure 5.2. Ash beds and XRF plots (5mm resolution). The boundary between the Buda Formation and the Lower Eagle Group (LEF), and the Upper Eagle Ford Group (UEF) are marked by solid line and dashed line, respectively.

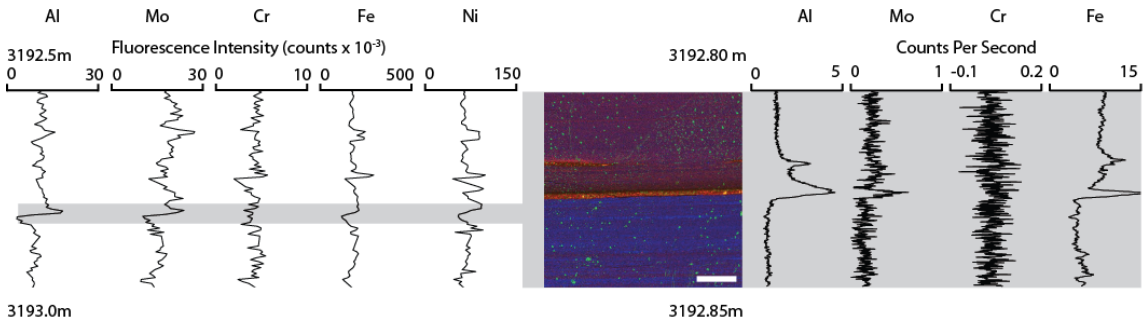

Figure 5.3. Selected ash bed region (gray) was scanned with high resolution (100 um) XRF. Blue is Ca, red is Fe, and green is S. Scale bar is 1 cm. Pyrite (yellow) presents within ash bed. The sulfur acne (green spots) spreading on XRF map is due to oil (high sulfur content) was spilled on the slab surface.

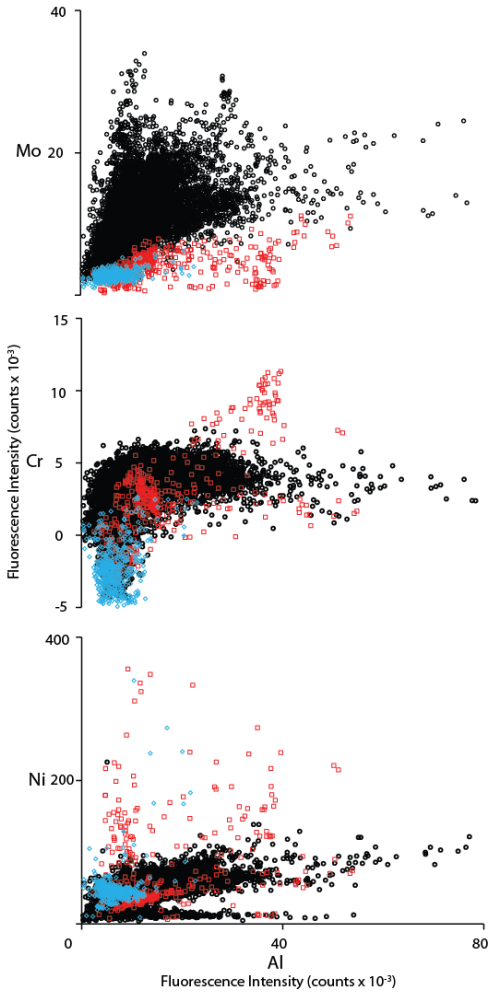

Figure 5.4. Normalizing Mo, Cr and Ni to Al were used to evaluate the redox condition and productivity in three units. Blue diamond represents the Buda Formation, black circle represents the Lower Eagle Ford Group, and red square represents the Upper Eagle Ford Group. Mo content is much higher in the Lower Eagle Ford Group than the other two units indicating the Lower Eagle Ford Group was deposited in a strong euxinic environments. Cr positively correlated with Al at low Al fluorescence and negatively correlated with Al at high Al fluorescence (see text). Highly variable of Ni suggests that Ni was not a major primary component of ashes prior to deposition.

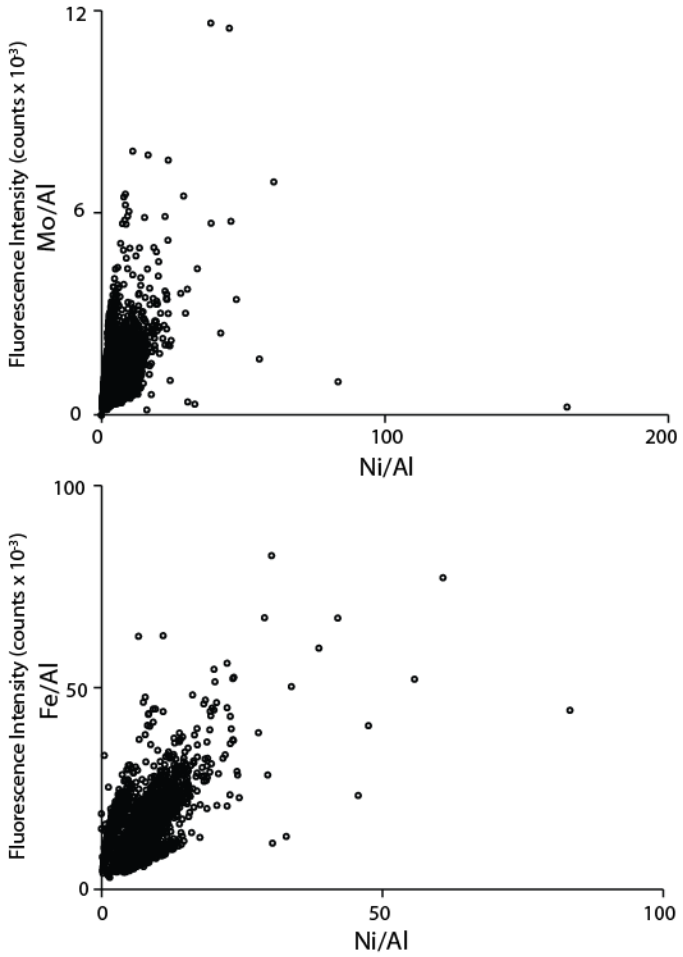

Figure 5.5. High productivity (high Ni/Al fluorescence ratio) is associated with more reducing conditions (high Mo/Al fluorescence ratio), and also is associated with more authigenic pyrite (high Fe/Al fluorescence ratio) in the Lower Eagle Ford.

CHAPTER VI

SUMMARY

Microbial iron reduction promoted precipitation of spherical calcium-rich siderite grains. Actively metabolizing cells locally raised *p*H and provided essential nucleation sites for carbonate precipitation. Precipitation only occurred when calcium was present in solution, possibly due to local adsorption of iron on cell walls or intracellular precipitation of iron oxides. High $[Mg^{2+}]/[Ca^{2+}]$ ratios inhibited carbonate precipitation and changed mineral compositions, but did not alter carbonate morphology. Extended incubations to three months altered carbonate compositions from $Ca_{0.16}Fe_{0.84}CO_3$ to $Ca_{0.4}Fe_{0.6}CO_3$. Because most mineral compositions observed are metastable at low temperature, they could act as precursors to calcite, siderite and dolomite. By modifying local *p*H, providing nucleation sites, and altering metal ions (e.g. Ca^{2+} and Fe^{2+}) composition around cell surfaces, iron reducing microorganisms could thus produce a wide range of carbonate cements in natural sediments, including some with relatively low iron content. Microbial iron reduction may therefore play a significant but largely hidden role in the sedimentary authigenic inorganic carbon sink.

Iron reducing physiologies, including membrane bound enzymes, electron shuttles and nanowires, apply different strategies to transfer electrons to solid iron minerals and thus regulate the morphology of precipitated carbonate and micropore formation. Iron reduction rate and location of iron reduction relative to the cell surface together determine the level of local saturation to precipitate corresponding carbonate

morphologies (rhombohedral or spherical). Long chained carbonate was only formed by *G. fermentans*, and its non-motile character and extracellular electron shuttle (riboflavin) is responsible for this special morphology. Micropores induced by different iron reducing physiologies, for instance, cell shaped and cave like micropores in iron oxide were formed by *S. oneidensis MR-1* and *G. metallireducens GS-15* respectively, and expansive cell shaped micropore in carbonate was formed by *G. fermentans*, can be a potent biosignature, because the type of micropore is not just recording microbial iron reduction but also correlates with a certain iron reducing physiology.

Ce(III) oxidation was mediated by *Roseobacter sp*. AzwK-3b through the production of extracellular superoxide. This suggests Ce oxidation could be associated with the distribution of superoxide producers in seawater. Ce(IV) was directly reduced by *Shewanella oneidensis MR-1*, as well as by Fe^{2+} and Mn^{2+} abiotically. Cerium undergoing reduction in the presence of Fe^{2+} and Mn^{2+} links the cerium reduction to microbial iron and manganese reduction. These results suggest that bacteria can directly or indirectly mediate cerium redox cycling.

The Late Cretaceous Eagle Ford Group (Cenomanian/Turonian) contains abundant volcanic ash beds interbedded with black argillaceous limestones and marls, providing opportunities for observation of the influence of ash on productivity and basin chemistry in the Western Interior Seaway. A 49-m-thick core sample containing 51 visualized ash beds with varying thickness was collected through the Lower Eagle Ford and the basal Upper Eagle Ford from south Texas was scanned by x-ray *fluorescence* spectroscopy to examine burial of Fe, trace elements delivered to the sediment by

sinking organic matter (Ni), and paleoredox proxies (Mo and Cr) below, in, and above ash beds. The results showe that ash beds and beds containing admixed ash contain much more Fe than interbedded black shales, suggesting that ash transported reactive Fe to otherwise Fe-poor settings. The contents of Mo and Ni were significantly greater in beds with admixed ash than in surrounding beds. In contrast, Cr was less abundant in the beds with greatest ash content. These observations imply that input of ash increased marine productivity (elevated Ni), which in turn enhanced oxygen demand and promoted euxinia (elevated Mo and lower Cr). We conclude that Fe-bearing volcanic ash fertilized the southern Cenomanian Western Interior Seaway.

This dissertation provides mineralogical, morphological and geochemical examples of cases in which that bacterial physiologies play critical roles in the precipitation/dissolution of minerals and in the redox cycling of trace and rare earth elements. By creating special physicochemical microenvironment, bacterial physiologies can produce distinctive minerals and chemical patterns, which may be preserved as biosignatures useful for identifying past life.

REFERENCES

Algeo, T. J., and Maynard, J. B., 2004, Trace-element behavior and redox facies in core shales of Upper Pennsylvanian Kansas-type cyclothems. Chemical Geology, v. 206, no. 3-4, p. 289-318.

Alibo, D. S., and Nozaki, Y., 1999, Rare earth elements in seawater: particle association, shale-normalization, and Ce oxidation. Geochimica et Cosmochimica Acta, v. 63, no. 3-4, p. 363-372.

Allentoft, M. E., Collins, M., Harker, D., Haile, J., Oskam, C. L., Hale, M. L., Campos, P. F., Samaniego, J. A., Gilbert, M. T. P., Willerslev, E., Zhang, G. J., Scofield, R. P., Holdaway, R. N., and Bunce, M., 2012, The half-life of DNA in bone. measuring decay kinetics in 158 dated fossils. Proceedings of the Royal Society B-Biological Sciences, v. 279, no. 1748, p. 4724-4733.

Behrenfeld, M. J., Bale, A. J., Kolber, Z. S., Aiken, J., and Falkowski, P. G., 1996, Confirmation of iron limitation of phytoplankton photosynthesis in the equatorial Pacific Ocean, Nature, v. 383, no. 6600, p. 508-511.

Berner, R. A., and Morse, J. W., 1974, Dissolution kinetics of calcium carbonate in seawater, IV theory of calcite dissolution. American Journal of Science, v. 274, no. 2, p. 108-134.

Blain, S., Queguiner, B., Armand, L., Belviso, S., Bombled, B., Bopp, L., Bowie, A., Brunet, C., Brussaard, C., Carlotti, F., Christaki, U., Corbiere, A., Durand, I., Ebersbach, F., Fuda, J. L., Garcia, N., Gerringa, L., Griffiths, B., Guigue, C., Guillerm, C., Jacquet, S., Jeandel, C., Laan, P., Lefevre, D., Lo Monaco, C., Malits, A., Mosseri, J., Obernosterer, I., Park, Y. H., Picheral, M., Pondaven, P., Remenyi, T., Sandroni, V., Sarthou, G., Savoye, N., Scouarnec, L., Souhaut, M., Thuiller, D., Timmermans, K., Trull, T., Uitz, J., van Beek, P., Veldhuis, M., Vincent, D., Viollier, E., Vong, L., and Wagener, T., 2007, Effect of natural iron fertilization on carbon sequestration in the Southern Ocean. Nature, v. 446, no. 7139, p. 1070-1071.

Bosak, T., and Newman, D. K., 2003, Microbial nucleation of calcium carbonate in the Precambrian. Geology, v. 31, no. 7, p. 577-580.

Brasier, M. D., Green, O. R., Jephcoat, A. P., Kleppe, A. K., Van Kranendonk, M. J., Lindsay, J. F., Steele, A., and Grassineau, N. V., 2002, Questioning the evidence for Earth's oldest fossils. Nature, v. 416, no. 6876, p. 76-81.

Buick, R., 1984, Carbonaceous filaments from North Pole, Western Australia: are they fossil bacteria in Archean stromatolites. Precambrian Research, v. 24, no. 2, p. 157-172.

Burdige, D. J., 1993, The biogeochemistry of manganese and iron reduction in marine sediments. Earth Science Reviews, v. 35, no. 3, p. 249-284.

Burton, W. K., Cabrera, N., and Frank, F. C., 1951, The growth of crystals and the equilibrium strucuture of their surfaces. Philosophical Transactions of the Royal Society of London Series A, Mathematical Physical and Engineering Sciences, v. A243, p. 299-358.

Canfield, D. E., Jorgensen, B. B., Fossing, H., Glud, R., Gundersen, J., Ramsing, N. B., Thamdrup, B., Hansen, J. W., Nielsen, L. P., and Hall, P. O., 1993, Pathways of organic carbon oxidation in three continental margin sediments. Marine Geology, v. 113, p. 27-40.

Canfield, D. E., Poulton, S. W., and Narbonne, G. M., 2007, Late Neoproterozoic deep ocean oxygenation and the rise of animal life. Science, v. 315, no. 5808, p. 92-95.

Canfield, D. E., and Raiswell, R., 1991, Carbonate precipitation and dissolution: its relevance to fossil preservation, *in* Allison, P. A., and Briggs, D. E. G., eds., Taphonomy: Releasing the Data Locked in the Fossil Record: London, Plenum, p. 411-453.

Chafetz, H. S., 2013, Porosity in bacterially induced carbonates: focus on micropores. AAPG Bulletin, v. 97, no. 11, p. 2103-2111.

Chernov, A. A., 1984, Modern crystallography III - crystal growth. Springer (Berlin), p. 517.

Coale, K. H., Johnson, K. S., Fitzwater, S. E., Gordon, R. M., Tanner, S., Chavez, F. P., Ferioli, L., Sakamoto, C., Rogers, P., Millero, F., Steinberg, P., Nightingale, P., Cooper, D., Cochlan, W. P., Landry, M. R., Constantinou, J., Rollwagen, G., Trasvina, A., and Kudela, R., 1996, A massive phytoplankton bloom induced by an ecosystem-scale iron fertilization experiment in the equatorial Pacific Ocean. Nature, v. 383, no. 6600, p. 495-501.

Coates, J. D., Ellis, D. J., Gaw, C. V., and Lovley, D. R., 1999, Geothrix fermentans gen. nov., sp nov., a novel Fe(III)-reducing bacterium from a hydrocarbon contaminated aquifer. International Journal of Systematic Bacteriology, v. 49, p. 1615-1622.

Coleman, M. L., 1985, Geochemistry of diagenetic non-silicate minerals: kinetic considerations: Transactions of the Royal Society of London, v. A315, p. 39-56.

Curtis, C. D., and Coleman, M.L., 1986, Controls on the precipitation of early diagenetic calcite, dolomite and siderite concretions in complex depositional sequences. The Society of Economic Paleontologists and Mineralogists (SEPM), Roles of Organic Matter in Sediment Diagenesis (SP38). p. 23-33.

Defarge, C., Trichet, J., Jaunet, A. M., Robert, M., Tribble, J., and Sansone, F. J., 1996, Texture of microbial sediments revealed by cryo-scanning electron microscopy. Journal of Sedimentary Research, v. 66, no. 5, p. 935-947.

Denne, R. A., Hinote, R. E., Breyer, J. A., Kosanke, T. H., Lees, J. A., Englehardt-Moore, N., Spaw, J. M., and Tur, M., 2014, The Cenomanian–Turonian Eagle Ford Group of South Texas: Insights on timing and paleoceanographic conditions from geochemistry and micropaleontologic analyses. Palaeogeography, Palaeoclimatology, Palaeoecology, v. 413, p. 2-28.

Devrind, J. P. M., Boogerd, F. C., and Devrinddejong, E. W., 1986, Manganese reduction by a marine bacillus species. Journal of Bacteriology, v. 167, no. 1, p. 30-34.

DiChristina, T. J., Moore, C. M., and Haller, C. A., 2002, Dissimilatory Fe(III) and Mn(IV) reduction by *Shewanella putrefaciens* requires *ferE*, a homolog of the *pulE (gspE)* type II protein secretion gene. Journal of Bacteriology, v. 184, no. 1, p. 142-151.

Duggen, S., Croot, P., Schacht, U., and Hoffmann, L., 2007, Subduction zone volcanic ash can fertilize the surface ocean and stimulate phytoplankton growth: evidence from biogeochemical experiments and satellite data. Geophysical Research Letters, v. 34, L01612.

Duggen, S., Olgun, N., Croot, P., Hoffmann, L., Dietze, H., Delmelle, P., and Teschner, C., 2010, The role of airborne volcanic ash for the surface ocean biogeochemical iron cycle: a review. Biogeosciences, v. 7, no. 3, p. 827-844.

Dupraz, C., Reid, R. P., Braissant, O., Decho, A. W., Norman, R. S., and Visscher, P. T., 2009, Processes of carbonate precipitation in modern microbial mats. Earth Science Reviews, v. 96, no. 3, p. 141-162.

Elderfield, H., 1988, The oceanic chemistry of the rare earth elements. Philosophical Transactions of the Royal Society of London Series A, Mathematical Physical and Engineering Sciences, v. 325, no. 1583, p. 105-126.

Falini, G., Fermani, S., Gazzano, M., and Ripamonti, A., 2000, Polymorphism and architectural crystal assembly of calcium carbonate in biologically inspired polymeric matrices. Journal of the Chemical Society Dalton Transactions, no. 21, p. 3983-3987.

Fernandez-Diaz, L., Putnis, A., Prieto, M., and Putnis, C. V., 1996, The role of magnesium in the crystallization of calcite and aragonite in a porous medium. Journal of Sedimentary Research, v. 66, no. 3, p. 482-491.

Fike, D. A., Grotzinger, J. P., Pratt, L. M., and Summons, R. E., 2006, Oxidation of the Ediacaran Ocean. Nature, v. 444, no. 7120, p. 744-747.

Froelich, P. N., Klinkhammer, G. P., Bender, M. L., Luedtke, N. A., Heath, G. R., Cullen, D., Dauphin, P., Hammond, D., Hartman, B., and Maynard, V., 1979, Early oxidation of organic matter in pelagic sediments of the eastern equatorial Atlantic: suboxic diagenesis. Geochimica et Cosmochimica Acta, v. 43, p. 1075-1090.

Frogner, P., Gislason, S. R., and Oskarsson, N., 2001, Fertilizing potential of volcanic ash in ocean surface water. Geology, v. 29, no. 6, p. 487-490.

Fu, Q. S., Boonchayaanant, B., Tang, W. P., Trost, B. M., and Criddle, C. S., 2009, Simple menaquinones reduce carbon tetrachloride and iron (III). Biodegradation, v. 20, no. 1, p. 109-116.

German, C. R., and Elderfield, H., 1989, Rare earth elements in Saanich Inlet, British-Columbia, a seasonally anoxic basin. Geochimica et Cosmochimica Acta, v. 53, no. 10, p. 2561-2571.

Gescher, J. S., Cordova, C. D., and Spormann, A. M., 2008, Dissimilatory iron reduction in *Escherichia coli*: identification of *CymA* of *Shewanella oneidensis* and *NapC* of *E.coli* as ferric reductases. Molecular Microbiology, v. 68, no. 3, p. 706-719.

Glasauer, S., Langley, S., and Beveridge, T. J., 2002, Intracellular iron minerals in a dissimilatory iron-reducing bacterium. Science, v. 295, no. 5552, p. 117-119.

Gluyas, J. G., 1984, Early carbonate diagenesis within Phanerozoic shales and sandstones of the NW European Shelf. Clay Minerals, v. 19, no. 3, p. 309-321.

Gonzalez, J. M., and Moran, M. A., 1997, Numerical dominance of a group of marine bacteria in the alpha-subclass of the class Proteobacteria in coastal seawater. Applied and Environmental Microbiology, v. 63, no. 11, p. 4237-4242.

Gustafsson, J. P., 2006, Visual MINTEQ 3.0 user guide. Capturado em de, v. 26.

Habicht, K. S., Gade, M., Thamdrup, B., Berg, P., and Canfield, D. E., 2002, Calibration of sulfate levels in the Archean Ocean. Science, v. 298, no. 5602, p. 2372-2374.

Hansel, C. M., Learman, D. R., Voelker, B. M., and Vazquez-Rodriguez, A. I., 2011, Formation of manganese oxides by bacterially generated superoxide. Nature Geoscience, v. 4, no. 2, p. 95-98.

Hashmi, M. H., and Rashid, A., 1966, Colorimetric determination of gold platinum and cerium. Analytical Chemistry, v. 38, no. 10, p. 1423-1424.

Heckert, E. G., Karakoti, A. S., Seal, S., and Self, W. T., 2008, The role of cerium redox state in the SOD mimetic activity of nanoceria, Biomaterials, v. 29, no. 18, p. 2705-2709.

Horita, J., and Berndt, M. E., 1999, Abiogenic methane formation and isotopic fractionation under hydrothermal conditions. Science, v. 285, no. 5430, p. 1055-1057.

Hutchins, D. A., and Bruland, K. W., 1998, Iron-limited diatom growth and Si : N uptake ratios in a coastal upwelling regime. Nature, v. 393, no. 6685, p. 561-564.

Jiang, W., Saxena, A., Song, B., Ward, B. B., Beveridge, T. J., and Myeni, S. C. B., 2004, Elucidation of functional groups on Gram-positive and Gram-negative bacterial surfaces using infrared spectroscopy. Langmuir, v. 20, p. 11433-11442.

Johnson, C. M., Beard, B. L., and Roden, E. E., 2008, The iron isotope fingerprints of redox and biogeochemical cycling in the modern and ancient Earth. Annual Review of Earth and Planetary Sciences, v. 36, p. 457-493.

Klein, C., and Beukes, N. J., 1989, Geochemistry and sedimentology of a facies transition from limestone to iron-formation deposition in the Early Proterozoic transvaal supergroup, South-Africa. Economic Geology, v. 84, no. 7, p. 1733-1774.

Klein, C., and Beukes, N. J., 1993, The Proterozoic biosphere - a multidisciplinary study. Cambridge University Press, v. 259, no. 5092, p. 142-143.

Knoll, A. H., Canfield, D. E., and Konhauser, K. O., 2012, Fundamentals of geobiology. John Wiley & Sons, p. 49-64.

Konhauser, K. O., Newman, D. K., and Kappler, A., 2005, The potential significance of microbial Fe(III) reduction during deposition of Precambrian banded iron formations. Geobiology, v. 3, no. 3, p. 167-177.

Krumbein, W. E., 1978, Photolithotrophic and chemoorganotrophic activity of bacteria and algae as related to beachrock formation and degradation (Gulf of Aqaba, Sinai). Geomicrobiology Journal, v. 1, p. 139-203.

Learman, D. R., Voelker, B. M., Vazquez-Rodriguez, A. I., and Hansel, C. M., 2011, Formation of manganese oxides by bacterially generated superoxide. Nature Geoscience, v. 4, no. 2, p. 95-98.

Lee, C. T. A., Shen, B., Slotnick, B. S., Liao, K., Dickens, G. R., Yokoyama, Y., Lenardic, A., Dasgupta, R., Jellinek, M., Lackey, J. S., Schneider, T., and Tice, M. M., 2013, Continental arc-island arc fluctuations, growth of crustal carbonates, and long-term climate change. Geosphere, v. 9, no. 1, p. 21-36.

Lovley, D. R., 1991, Dissimilatory Fe(III) and Mn(IV) reduction. Microbiological Reviews, v. 55, no. 2, p. 259-287.

Lovley, D. R., Phillips, E. J. P., and Lonergan, D. J., 1989, Hydrogen and formate oxidation coupled to dissimilatory reduction of iron or manganese by *Alteromonas putrefaciens*. Applied and Environmental Microbiology, v. 55, no. 3, p. 700-706.

Lowe, D. R., 1999, Petrology and sedimentology of cherts and related silicified sedimentary rocks in the Swaziland Supergroup. Geological Society of America Special Paper 329, p. 83-114.

Marsili, E., Baron, D. B., Shikhare, I. D., Coursolle, D., Gralnick, J. A., and Bond, D. R., 2008, *Shewanella* secretes flavins that mediate extracellular electron transfer. Proceedings of the National Academy of Sciences of the United States of America, v. 105, no. 10, p. 3968-3973.

Martin, J. H., Coale, K. H., Johnson, K. S., Fitzwater, S. E., Gordon, R. M., Tanner, S. J., Hunter, C. N., Elrod, V. A., Nowicki, J. L., Coley, T. L., Barber, R. T., Lindley, S., Watson, A. J., Vanscoy, K., Law, C. S., Liddicoat, M. I., Ling, R., Stanton, T., Stockel, J., Collins, C., Anderson, A., Bidigare, R., Ondrusek, M., Latasa, M., Millero, F. J., Lee, K., Yao, W., Zhang, J. Z., Friederich, G., Sakamoto, C., Chavez, F., Buck, K., Kolber, Z., Greene, R., Falkowski, P., Chisholm, S. W., Hoge, F., Swift, R., Yungel, J., Turner, S., Nightingale, P., Hatton, A., Liss, P., and Tindale, N. W., 1994, Testing the iron hypothesis in ecosystems of the equatorial Pacific-Ocean. Nature, v. 371, no. 6493, p. 123-129.

McHargue, T. R., and Price, R. C., 1982, Dolomite from clay in argillaceous or shale associated marine carbonates. Journal of Sedimentary Petrology, v. 52, no. 3, p. 873-886.

Medalia, A. I., and Byrne, B. J., 1951, Spectrophotometric determination of cerium(IV). Analytical Chemistry, v. 23, no. 3, p. 453-456.

Mehta-Kolte, M. G., and Bond, D. R., 2012, *Geothrix fermentans* secretes two different redox active compounds to utilize electron acceptors across a wide range of redox potentials. Applied and Environmental Microbiology, v. 78, no. 19, p. 6987-6995.

Meister, P., 2013, Two opposing effects of sulfate reduction on carbonate precipitation in normal marine, hypersaline, and alkaline environments. Geology, v. 41, no. 4, p. 499-502.

Moffett, J. W., 1990, Microbially mediated cerium oxidation in sea water. Nature, v. 345, no. 6274, p. 421-423.

Moffett, J. W., 1994, The relationship between cerium and manganese oxidation in the marine-environment. Limnology and Oceanography, v. 39, no. 6, p. 1309-1318.

Morse, J. W., 1978, Dissolution kinetics of calcium carbonate in seawater: 6. near equilibrium dissolution kinetics of calcium carbonate-rich deep-sea sediments. American Journal of Science, v. 278, no. 3, p. 344-353.

Morse, J. W., Wang, Q. W., and Tsio, M. Y., 1997, Influences of temperature and Mg:Ca ratio on $CaCO_3$ precipitates from seawater. Geology, v. 25, no. 1, p. 85-87.

Mortimer, R. J. G., Coleman, M. L., and Rae, J. E., 1997, Effect of bacteria on the elemental composition of early diagenetic siderite: implications for palaeoenvironmental interpretations. Sedimentology, v. 44, no. 4, p. 759-765.

Mozley, P. S., and Carothers, W. W., 1992, Elemental and isotopic composition of siderite in the kuparuk formation, alaska: effect of microbial activity and water sediment interaction on early pore-water chemistry. Journal of Sedimentary Petrology, v. 62, no. 4, p. 681-692.

Mucci, A., and Morse, J. W., 1983, The Incorporation of Mg^{2+} and Sr^{2+} into calcite overgrowths: influences of growth-rate and solution composition. Geochimica et Cosmochimica Acta, v. 47, no. 2, p. 217-233.

Nash, A. J., and Pittman, E. D., 1975, Ferro-magnesian calcite cement in sandstones. Journal of Sedimentary Petrology, v. 45, no. 1, p. 258-265.

Nealson, K. H., and Myers, C. R., 1990, Iron reduction by bacteria: a potential role in the genesis of banded iron formations. American Journal of Science, v. 290A, p. 35-45.

Nevin, K. P., and Lovley, D. R., 2002, Mechanisms for accessing insoluble Fe(III) oxide during dissimilatory Fe(III) reduction by *Geothrix fermentans*. Applied and Environmental Microbiology, v. 68, no. 5, p. 2294-2299.

Poulton, S. W., and Raiswell, R., 2002, The low-temperature geochemical cycle of iron: From continental fluxes to marine sediment deposition. American Journal of Science, v. 302, no. 9, p. 774-805.

Pye, K., Dickson, J. A. D., Schiavon, N., Coleman, M. L., and Cox, M., 1990, Formation of siderite-Mg-calcite-iron sulfide concretions in intertidal marsh and sandflat Sediments, North-Norfolk, England. Sedimentology, v. 37, no. 2, p. 325-343.

Ramos, A. R., Keller, K. L., Wall, J. D., and Pereira, I. A. C., 2012, The membrane QmoABC complex interacts directly with the dissimilatory adenosine 5 '-phosphosulfate reductase sulfate reducing bacteria. Frontiers in Microbiology, v. 3, p. 137.

Reguera, G., McCarthy, K. D., Mehta, T., Nicoll, J. S., Tuominen, M. T., and Lovley, D. R., 2005, Extracellular electron transfer via microbial nanowires. Nature, v. 435, no. 7045, p. 1098-1101.

Reid, R. P., Visscher, P. T., Decho, A. W., Stolz, J. F., Bebout, B. M., Dupraz, C., Macintyre, I. G., Paerl, H. W., Pinckney, J. L., Prufert-Bebout, L., Steppe, T. F., and DesMarais, D. J., 2000, The role of microbes in accretion, lamination and early lithification of modern marine stromatolites. Nature, v. 406, no. 6799, p. 989-992.

Richard, J., 1983, Carbonates: mineralogy and chemistry. Reviews in Mineralogy, v. 11, p. 247.

Richard, L., 1978, A chemical model for calcite crystal growth and morphology control. Journal of Sedimentary Petrology, v. 48, p. 337-344.

Ries, J. B., Anderson, M. A., and Hill, R. T., 2008, Seawater Mg/Ca controls polymorph mineralogy of microbial $CaCO_3$: a potential proxy for calcite-aragonite seas in Precambrian time. Geobiology, v. 6, no. 2, p. 106-119.

Roden, E. E., and Ferris, F. G., 2000, Preprints of extended abstracts. 220th ACS National Meeting, v. 40, no. 20, p. 400-403.

Romanek, C. S., Jimenez-Lopez, C., Navarro, A. R., Sanchez-Roman, M., Sahai, N., and Coleman, M., 2009, Inorganic synthesis of Fe-Ca-Mg carbonates at low temperature. Geochimica et Cosmochimica Acta, v. 73, no. 18, p. 5361-5376.

Rose, A. L., Webb, E. A., Waite, T. D., and Moffett, J. W., 2008, Measurement and implications of nonphotochemically generated superoxide in the equatorial Pacific Ocean. Environmental Science & Technology, v. 42, no. 7, p. 2387-2393.

Rusak, S. A., Peake, B. M., Richard, L. E., Nodder, S. D., and Cooper, W. J., 2011, Distributions of hydrogen peroxide and superoxide in seawater east of New Zealand. Marine Chemistry, v. 127, no. 1-4, p. 155-169.

Schopf, J. W., and Walter, M.R., 1983, Archean microfossils: new evidence of ancient microbes, *In* Schopf, J.W. eds., Earth's earliest biosphere. Princeton University Press, Princeton, New Jersey, p. 214-239.

Schrag, D. P., Higgins, J. A., Macdonald, F. A., and Johnston, D. T., 2013, Authigenic carbonate and the history of the global carbon cycle. Science, v. 339, no. 6119, p. 540-543.

Sholkovitz, E. R., and Schneider, D. L., 1991, Cerium redox cycles and rare earth elements in the sargasso sea. Geochimica et Cosmochimica Acta, v. 55, no. 10, p. 2737-2743.

Templeton, A. S., Staudigel, H., and Tebo, B. M., 2005, Diverse Mn(II)-oxidizing bacteria isolated from submarine basalts at Loihi Seamount. Geomicrobiology Journal, v. 22, no. 3-4, p. 127-139.

Thompson, J. B., and Ferris, F. G., 1990, Cyanobacterial precipitation of gypsum, calcite, and magnesite from natural alkaline lake water. Geology, v. 18, no. 10, p. 995-998.

Tremblay, P. L., Aklujkar, M., Leang, C., Nevin, K. P., and Lovley, D., 2012, A genetic system for *Geobacter metallireducens*: role of the flagellin and pilin in the reduction of Fe(III) oxide. Environmental Microbiology Reports, v. 4, no. 1, p. 82-88.

Tribovillard, N., Algeo, T. J., Lyons, T., and Riboulleau, A., 2006, Trace metals as paleoredox and paleoproductivity proxies: an update. Chemical Geology, v. 232, no. 1-2, p. 12-32.

Van Lith, Y., Warthmann, R., Vasconcelos, C., and McKenzie, J. A., 2003, Microbial fossilization in carbonate sediments: a result of the bacterial surface involvement in dolomite precipitation. Sedimentology, v. 50, no. 2, p. 237-245.

Vermilyea, A. W., Hansard, S. P., and Voelker, B. M., 2010, Dark production of hydrogen peroxide in the Gulf of Alaska. Limnology and Oceanography, v. 55, no. 2, p. 580-588.

Viollier, E., Inglett, P. W., Hunter, K., Roychoudhury, A. N., and Van Cappellen, P., 2000, The ferrozine method revisited: Fe(II)/Fe(III) determination in natural waters. Applied Geochemistry, v. 15, no. 6, p. 785-790.

Visscher, P. T., Reid, R. P., and Bebout, B. M., 2000, Microscale observations of sulfate reduction: correlation of microbial activity with lithified micritic laminae in modern marine stromatolites. Geology, v. 28, no. 10, p. 919-922.

Waldo, R. A., Militello, M. C., and Gaarenstroom, S. W., 1993, Quantitative thin-film analysis with an energy-dispersive x-ray-detector. Surface and Interface Analysis, v. 20, no. 2, p. 111-114.

Walker, J. C. G., 1984, Suboxic diagenesis in banded iron formations. Nature, v. 309, no. 5966, p. 340-342.

Walsh, M. M., and Lowe, D. R., 1999, Modes of accumulation of carbonaceous matter in the early Archean: A petrographic and geochemical study of the carbonaceous cherts of the Swaziland Supergroup. Geological Society of America Special Paper 329, p. 115-132.

Warthmann, R., van Lith, Y., Vasconcelos, C., McKenzie, J. A., and Karpoff, A. M., 2000a, Bacterially induced dolomite precipitation in anoxic culture experiments. Geology, v. 28, p. 919-922.

Warthmann, R., Van Lith, Y., Vasconcelos, C., McKenzie, J. A., and Karpoff, A. M., 2000b, Bacterially induced dolomite precipitation in anoxic culture experiments. Geology, v. 28, no. 12, p. 1091-1094.

Watson, A. J., Bakker, D. C. E., Ridgwell, A. J., Boyd, P. W., and Law, C. S., 2000, Effect of iron supply on Southern Ocean CO_2 uptake and implications for glacial atmospheric CO_2. Nature, v. 407, no. 6805, p. 730-733.

Webb, A. D., Dickens, G. R., and Oliver, N. H. S., 2004, Carbonate alteration of the Upper Mount McRae Shale beneath the martite-microplaty hematite ore deposit at Mount Whaleback, Western Australia. Mineralium Deposita, v. 39, no. 5-6, p. 632-645.

Weber, K. A., Achenbach, L. A., and Coates, J. D., 2006, Microorganisms pumping iron: anaerobic microbial iron oxidation and reduction. Nature Reviews Microbiology, v. 4, no. 10, p. 752-764.

Weiner, S., and Dove, P. M., 2003, An overview of biomineralization processes and the problem of the vital effect. Biomineralization, v. 54, p. 1-29.

Wells, M. L., 2003, The level of iron enrichment required to initiate diatom blooms in HNLC waters. Marine Chemistry, v. 82, no. 1-2, p. 101-114.

Werner, S., and James, M., 1996, Aquatic Chemistry: chemical equilibria and rates in nature waters, 3rd Edition. Wiley Interscience, p. 330-331.

Woods, T. L., and Garrels, R. M., 1992, Calculated aqueous-solution-solid-solution relations in the low-temperature system CaO-MgO-FeO-CO_2-H_2O. Geochimica et Cosmochimica Acta, v. 56, no. 8, p. 3031-3043.

Wright, D. T., 1999, The role of sulphate-reducing bacteria and cyanobacteria in dolomite formation in distal ephemeral lakes of the Coorong region, South Australia. Sedimentary Geology, v. 126, p. 147-157.

Wright, J., Schrader, H., and Holser, W. T., 1987, Paleoredox variations in ancient oceans recorded by rare earth elements in fossil apatite. Geochimica et Cosmochimica Acta, v. 51, no. 3, p. 631-644.

Xiong, Y. J., Shi, L., Chen, B. W., Mayer, M. U., Lower, B. H., Londer, Y., Bose, S., Hochella, M. F., Fredrickson, J. K., and Squier, T. C., 2006, High affinity binding and direct electron transfer to solid metals by the *Shewanella oneidensis MR-1* outer membrane c-type cytochrome *OmcA*. Journal of the American Chemical Society, v. 128, no. 43, p. 13978-13979.

Zeng, Z., and Tice, M. M., 2014, Promotion and nucleation of carbonate precipitation during microbial iron reduction. Geobiology, v. 12, no. 4, p. 362-371.

APPENDIX: MODEL DEVELOPMENT

S. oneidensis MR-1 oxidizes lactate to acetate during iron reduction (Eq. A1) (Lovley et al., 1989).

$$4Fe(OH)_3 + CH_3CHOHCOO^- + 7H^+ \rightarrow 4Fe^{2+} + HCO_3^- + CH_3COO^- + 10H_2O \quad (A1)$$

In order to model this reaction, the reaction progress, *x*, was defined as the total amount of iron reduced or four times the amount of lactate reduced to acetate (Eq. A2).

$$x = \left[Fe^{2+}\right] + \left[FeHCO_3^+\right] = 4([CH_3COO^-] + [CH_3COOH]) = 4([CH_3CHOHCOOH]_{T0} - [CH_3CHOHCOOH] - [CH_3CHOHCOO^-]) \quad (A2)$$

Charge balance during this reaction then requires that the net charge of the medium not change as *x* increases (Eq. A3). Note that concentrations of species that do not change or species present in negligible concentrations are not included.

$$\frac{d}{dx}\left([H^+] + 2\left[Fe^{2+}\right] + \left[FeHCO_3^+\right] + 2\left[Ca^{2+}\right] - [OH^-] - [HCO_3^-] - 2[CO_3^{2-}] - [CH_3CHOHCOO^-] - [CH_3COO^-]\right) = 0 \quad (A3)$$

Together with equations describing speciation (Eqs. A4-A9) and mass balance (Eqs. A2 and A10), the dynamic behavior of the experimental system can be completely described.

$$[H^+][OH^-] = K_w \quad (A4)$$

$$\frac{[H^+][HCO_3^-]}{[H_2CO_3^*]} = K_{a1} \quad (A5)$$

$$\frac{[H^+][CO_3^{2-}]}{[HCO_3^-]} = K_{a2} \quad (A6)$$

$$\frac{[\mathrm{FeHCO_3^+}]}{[\mathrm{Fe^{2+}}][\mathrm{HCO_3^-}]} = K_{Fe} \quad \text{(A7)}$$

$$\frac{[\mathrm{H^+}][\mathrm{CH_3CHOHCOO^-}]}{[\mathrm{CH_3CHOHCOOH}]} = K_{la} \quad \text{(A8)}$$

$$\frac{[\mathrm{H^+}][\mathrm{CH_3COO^-}]}{[\mathrm{CH_3COOH}]} = K_{aa} \quad \text{(A9)}$$

$$[\mathrm{H_2CO_3^*}] = K_H p\mathrm{CO_2} \quad \text{(A10)}$$

For convenience, the constant LA_{T0} is introduced to indicate the initial concentration of lactate. Then the concentrations of lactate and acetate are described by Equations A11 and A12, respectively.

$$[\mathrm{CH_3CHOHCOO^-}] = (\mathrm{LA}_{T0} - \frac{x}{4}) \frac{K_{la}}{K_{la}+[\mathrm{H^+}]} \quad \text{(A11)}$$

$$[\mathrm{CH_3COO^-}] = \frac{x}{4} \frac{K_{aa}}{K_{aa}+[\mathrm{H^+}]} \quad \text{(A12)}$$

Substituting into the charge balance equation (Eq. A3) yields Equation A13.

$$\frac{d[\mathrm{H^+}]}{dx} + 1 + \frac{1}{1+K_{Fe}[\mathrm{HCO_3^-}]} + \frac{x[\mathrm{HCO_3^-}]}{[\mathrm{H^+}](1+K_{Fe}[\mathrm{HCO_3^-}])^2} \frac{d[\mathrm{H^+}]}{dx} + 2\frac{d[\mathrm{Ca^{2+}}]}{dx} + \frac{[\mathrm{OH^-}]}{[\mathrm{H^+}]} \frac{d[\mathrm{H^+}]}{dx} +$$

$$\frac{[\mathrm{HCO_3^-}]}{[\mathrm{H^+}]} \frac{d[\mathrm{H^+}]}{dx} + 4\frac{[\mathrm{CO_3^{2-}}]}{[\mathrm{H^+}]} \frac{d[\mathrm{H^+}]}{dx} + \frac{1}{4} \frac{K_{la}}{K_{la}+[\mathrm{H^+}]} + \frac{(\mathrm{LA}_{T0}-\frac{x}{4})K_{la}}{(K_{la}+[\mathrm{H^+}])^2} \frac{d[\mathrm{H^+}]}{dx} - \frac{1}{4} \frac{K_{aa}}{K_{aa}+[\mathrm{H^+}]} +$$

$$\frac{xK_{aa}}{4(K_{aa}+[\mathrm{H^+}])^2} \frac{d[\mathrm{H^+}]}{dx} = 0 \quad \text{(A13)}$$

Collecting terms including $d[\mathrm{H+}]/dx$ to the left side of the equation yields Equation A14.

$$-\frac{1}{[\mathrm{H^+}]}\frac{d[\mathrm{H^+}]}{dx}\left([\mathrm{H^+}]+\frac{x[\mathrm{HCO_3^-}]}{(1+K_{Fe}[\mathrm{HCO_3^-}])^2}+[\mathrm{OH^-}]+[\mathrm{HCO_3^-}]+4[\mathrm{CO_3^{2-}}]+\right.$$

$$\left.\frac{[\mathrm{H^+}](\mathrm{LA}_{T0}-\frac{x}{4})K_{la}}{(K_{la}+[\mathrm{H^+}])^2}+\frac{[\mathrm{H^+}]xK_{aa}}{4(K_{aa}+[\mathrm{H^+}])^2}\right)=1+2\frac{d[\mathrm{Ca^{2+}}]}{dx}+\frac{1}{1+K_{Fe}[\mathrm{HCO_3^-}]}+\frac{1}{4}\frac{K_{la}}{K_{la}+[\mathrm{H^+}]}-$$

$$\frac{1}{4}\frac{K_{aa}}{K_{aa}+[\mathrm{H^+}]} \qquad \text{(A14)}$$

Finally, because *p*H = $\log_{10}$ [H^+], this relationship can be rewritten to describe the rate of change of *p*H with respect to *x* (Eq. A15).

$$\frac{d\mathrm{pH}}{dx}=\frac{1}{\ln(10)}\left(1+2\frac{d[\mathrm{Ca^{2+}}]}{dx}+\frac{1}{1+K_{Fe}[\mathrm{HCO_3^-}]}+\frac{1}{4}\frac{K_{la}}{K_{la}+[\mathrm{H^+}]}-\frac{1}{4}\frac{K_{aa}}{K_{aa}+[\mathrm{H^+}]}\right)\cdot$$

$$\left([\mathrm{H^+}]+\frac{x[\mathrm{HCO_3^-}]}{(1+K_{Fe}[\mathrm{HCO_3^-}])^2}+[\mathrm{OH^-}]+[\mathrm{HCO_3^-}]+4[\mathrm{CO_3^{2-}}]+\frac{[\mathrm{H^+}](\mathrm{LA}_{T0}-\frac{x}{4})K_{la}}{(K_{la}+[\mathrm{H^+}])^2}+\right.$$

$$\left.\frac{[\mathrm{H^+}]xK_{aa}}{4(K_{aa}+[\mathrm{H^+}])^2}\right)^{-1} \qquad \text{(A15)}$$

This equation, combined with a model describing the evolution of [Ca^{2+}] (e.g. Eqs. 2.5 and 2.6) and the initial *p*H, completely describes the evolution of the model system. Note that, for *p*H ≥ 4.31, the terms in the numerator of Equation A15 resulting from *p*H forcing due to conversion of lactate into acetate decrease with decreasing [H^+] (increasing *p*H). Therefore, for experiments in which *p*H ≈ 7, equation A16 describes the maximum effect of organic substrate conversion.

$$\frac{1}{4}\frac{K_{la}}{K_{la}+[\mathrm{H^+}]}-\frac{1}{4}\frac{K_{aa}}{K_{aa}+[\mathrm{H^+}]}\leq 1.25\times10^{-3} \qquad \text{(A16)}$$

Because this effect is small relative to the other terms in the numerator of Equation A15, conversion of lactate to acetate can be neglected.

The acid/base buffering strength of lactate and acetate can also be evaluated relative to other buffers in the medium by comparing terms in the denominator of

equation A15. In particular, the ratio of acetate and lactate buffer strength to bicarbonate buffer strength is described by equation A17.

$$\frac{1}{[\mathrm{HCO_3^-}]}\left(\frac{[\mathrm{H^+}](\mathrm{LA}_{T0}-\frac{x}{4})K_{la}}{(K_{la}+[\mathrm{H^+}])^2}+\frac{[\mathrm{H^+}]xK_{aa}}{4(K_{aa}+[\mathrm{H^+}])^2}\right)$$

$$=\frac{[\mathrm{H^+}]^2}{K_H p\mathrm{CO_2} K_{a1}}\left[\frac{(\mathrm{LA}_{T0}-\frac{x}{4})K_{la}}{(K_{la}+[\mathrm{H^+}])^2}+\frac{xK_{aa}}{4(K_{aa}+[\mathrm{H^+}])^2}\right] \quad \text{(A17)}$$

Through the course of an experiment (pH ≈ 7, LA_{T0} = 20 mM, 0 mM ≤ x ≤ 5 mM), this ratio is always less than 8.02×10^{-4}, implying that buffering by acetate and lactate is negligible compared to buffering by bicarbonate.

Because the conversion of lactate into acetate does not significantly drive changes in *p*H, nor does the presence of either significantly buffer the experimental medium, the system closely approximates the more generalized case of complete oxidation of organic matter to bicarbonate (Eq. 2.3).